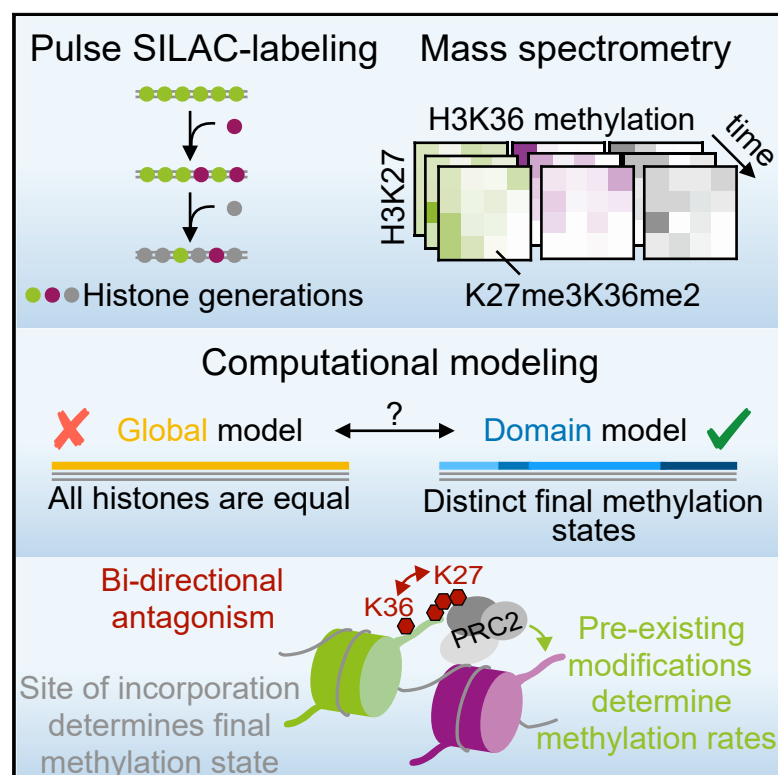


# Cell Reports

## Domain Model Explains Propagation Dynamics and Stability of Histone H3K27 and H3K36 Methylation Landscapes

### Graphical Abstract



### Authors

Constance Alabert, Carolin Loos, Moritz Voelker-Albert, ..., Carsten Marr, Axel Imhof, Anja Groth

### Correspondence

calabert@dundee.ac.uk (C.A.), carsten.marr@helmholtz-muenchen.de (C.M.), imhof@lmu.de (A.I.), anja.groth@bric.ku.dk (A.G.)

### In Brief

Alabert et al. introduce a computational model to describe the propagation of histone K27 and K36 methylations on successive generations of histones. This quantitative model invokes the existence of domains with distinct methylation endpoints and reveals that antagonisms between histone methylations enhance the stability of epigenetic states.

### Highlights

- Quantitative analysis of K27 and K36 methylation over several histone generations
- Computational model invokes the existence of distinct methylation state domains
- K27me3 on pre-existing histones stimulates the rate of *de novo* K27me3 establishment
- K27/K36 methylation antagonism enhances stability of epigenetic states



Alabert et al., 2020, Cell Reports 30, 1223–1234  
January 28, 2020 © 2020 The Authors.  
<https://doi.org/10.1016/j.celrep.2019.12.060>

CellPress

# Domain Model Explains Propagation Dynamics and Stability of Histone H3K27 and H3K36 Methylation Landscapes

Constance Alabert,<sup>1,7,9,\*</sup> Carolin Loos,<sup>2,3,9</sup> Moritz Voelker-Albert,<sup>4,8,9</sup> Simona Graziano,<sup>1,5</sup> Ignasi Forné,<sup>4</sup> Nazaret Reveron-Gomez,<sup>1,5</sup> Lea Schuh,<sup>2,3</sup> Jan Hasenauer,<sup>2,3,6</sup> Carsten Marr,<sup>2,\*</sup> Axel Imhof,<sup>4,\*</sup> and Anja Groth<sup>1,5,10,\*</sup>

<sup>1</sup>Biotech Research and Innovation Centre (BRIC), University of Copenhagen, Faculty of Health Sciences, University of Copenhagen, 2200 Copenhagen, Denmark

<sup>2</sup>Helmholtz Zentrum München-German Research Center for Environmental Health, Institute of Computational Biology, Neuherberg 85764, Germany

<sup>3</sup>Mathematical Modeling of Biological Systems, Center for Mathematics, Technische Universität München, Garching 85748, Germany

<sup>4</sup>Biomedical Center, Chromatin Proteomics Group, Department of Molecular Biology, Faculty of Medicine, Ludwig-Maximilians-Universität München, Großhaderner Strasse 9, 82152 Planegg-Martinsried, Germany

<sup>5</sup>The Novo Nordisk Center for Protein Research (CPR), Faculty of Health Sciences, University of Copenhagen, 2200 Copenhagen, Denmark

<sup>6</sup>Faculty of Mathematics and Natural Sciences, University of Bonn, 53115 Bonn, Germany

<sup>7</sup>Present address: Genome Regulation and Expression, School of Life Sciences, MSI/WTB Complex, University of Dundee, DD15EH Dundee, UK

<sup>8</sup>Present address: EpiQMax GmbH, Großhaderner Strasse 9, 82152 Planegg-Martinsried, Germany

<sup>9</sup>These authors contributed equally

<sup>10</sup>Lead Contact

\*Correspondence: [calabert@dundee.ac.uk](mailto:calabert@dundee.ac.uk) (C.A.), [carsten.marr@helmholtz-muenchen.de](mailto:carsten.marr@helmholtz-muenchen.de) (C.M.), [imhof@lmu.de](mailto:imhof@lmu.de) (A.I.), [anja.groth@bric.ku.dk](mailto:anja.groth@bric.ku.dk) (A.G.)

<https://doi.org/10.1016/j.celrep.2019.12.060>

## SUMMARY

Chromatin states must be maintained during cell proliferation to uphold cellular identity and genome integrity. Inheritance of histone modifications is central in this process. However, the histone modification landscape is challenged by incorporation of new unmodified histones during each cell cycle, and the principles governing heritability remain unclear. We take a quantitative computational modeling approach to describe propagation of histone H3K27 and H3K36 methylation states. We measure combinatorial H3K27 and H3K36 methylation patterns by quantitative mass spectrometry on subsequent generations of histones. Using model comparison, we reject active global demethylation and invoke the existence of domains defined by distinct methylation endpoints. We find that H3K27me3 on pre-existing histones stimulates the rate of *de novo* H3K27me3 establishment, supporting a read-write mechanism in timely chromatin restoration. Finally, we provide a detailed quantitative picture of the mutual antagonism between H3K27 and H3K36 methylation and propose that it stabilizes epigenetic states across cell division.

## INTRODUCTION

Most cells in a multicellular organism can be functionally very distinct despite the fact that they share the same genomic

information. Cellular specialization during development is based on the ability to establish, maintain, and execute different gene expression programs. How transcriptional programs are established during development and maintained in cycling cells is a fundamental question in biology. Chromatin organization plays a fundamental role in this process, but it remains unclear how specific chromatin states are stably inherited from a mother cell to its daughters. Histone post-translational modifications are highly cell-type specific and constitute an important level of chromatin regulation that controls transcription programs. Histone modifications can be inherited from mother cells through DNA replication and mitosis to daughter cells, but the mechanisms underlying this inheritance are still not fully understood.

During DNA replication, old histones H3-H4 are evicted from the parental strand and re-deposited onto the two daughter DNA strands. Histone acetylation and methylation marks are maintained on the old histones during this recycling process (Alabert et al., 2015; Scharf et al., 2009; Xu et al., 2012). Recycling is accurate and almost symmetric, such that positional information is maintained and the two strands receive close-to-equal contributions of old modified histones (Petryk et al., 2018; Reveron-Gomez et al., 2018; Yu et al., 2018). In parallel, newly synthesized histones are deposited to maintain nucleosome density. Because new histones are largely unmodified, except from transient di-acetylation on histone H4, histone methylation levels are diluted 2-fold on the daughter strands as compared to parental chromatin. To maintain chromatin states across cell division, new histones become modified to resemble their neighboring old histones. This process of chromatin restoration is highly heterogeneous, taking place across the full cell cycle with modification and locus-specific kinetics (Alabert et al., 2015; Reveron-Gomez et al., 2018).



Despite major advances in understanding histone dynamics coupled to DNA replication, the picture remains rudimentary with respect to the mechanisms that govern restoration and thus heritability of modifications. This partly reflects the complexity in the regulation of histone modifications, involving positive and negative cross-talk among modifications themselves and with other chromatin features (e.g., DNA methylation and sequence elements) and processes (e.g., transcription). A favored paradigm for inheritance of the repressive modifications, H3K9me3 and H3K27me3, is self-propagation through a read-write mechanism where the enzymes are activated by the presence of the modification on nearby nucleosomes (Reinberg and Vales, 2018). Structural and biochemical evidence strongly support a read-write mechanism in H3K9me3 and H3K27me3 establishment and spreading (Allshire and Madhani, 2018; Reinberg and Vales, 2018): enhancer of zeste homolog 2 (EZH2), the catalytic subunit of polycomb repressive complex 2 (PRC2) that mediates mono-, di-, and tri-methylation of H3K27 (from here on denoted as K27me1/2/3) is allosterically activated by binding of pre-existing K27me3 to an aromatic cage in the embryonic ectoderm development (EED) subunit (Reinberg and Vales, 2018). This can work in *trans* between neighboring nucleosomes (Poepfel et al., 2018) and could allow K27me3 on recycled old histones to instruct establishment of K27me3 on new histones after DNA replication (Reinberg and Vales, 2018). Consistent with this, EED cage mutations that abrogate allosteric activation reduce K27me3 levels and spreading (Lee et al., 2018; Oksuz et al., 2018). Intriguingly, PRC2 also methylates its binding partner JARID2 on a K27 mimicking peptide that also can activate the enzyme allosterically (Sanulli et al., 2015). However, other factors including genomic features, RNA and H2A K119 ubiquitination by polycomb repressive complex 1 (PRC1), can also contribute to PRC2 recruitment and deposition of H3K27me3 (Blackledge et al., 2014; Cooper et al., 2014; King et al., 2018; Laugesen et al., 2019; Yu et al., 2019). In *Drosophila*, self-propagation is not sufficient for K27me3 maintenance as sequence elements directing PRC1/2 recruitment are also required (Coleman and Struhl, 2017; Laprell et al., 2017). In mammalian cells, CpG richness is important for PRC2 recruitment, but a distinct recognition element remains to be identified (Laugesen et al., 2019). However, reintroduction of PRC2 into embryonic stem cells (ESCs) devoid of K27 methylation fully restores the K27me3 landscape (Højfeldt et al., 2018; Oksuz et al., 2018). This argues against a critical role for allosteric activation in establishment, but its importance in K27me3 maintenance remains debated.

K27me shows an intriguing interplay with methylation of K36, located in close vicinity on the H3 tail. H3K36 mono-, di-, and tri-methylation (from here on called K36me1/2/3) occupy distinct regions of the genome, much like K27me1/2/3, but is linked to transcription rather than repression. K36me2 is imposed by NSD1-3 and ASH1/1L and broadly distributed across the genome, including genic and intergenic regions. K36me3 is imposed by a single enzyme, SETD2, over gene bodies and promotes transcription fidelity by restoring a non-permissive chromatin state following RNA Pol II passage (Huang and Zhu, 2018). Consistent with their opposite roles in transcription, K36me3 and K27me3 are mutually exclusively distributed along

chromosomes (Ernst and Kellis, 2010; Streubel et al., 2018). Intriguingly, deregulation of these modifications can give rise to similar clinical outcomes, as Weaver syndromes (missense mutations in PRC2 subunits) and Sotos syndromes (loss-of-function mutations or deletions in NSD1 or SETD2) largely phenocopy each other (Tatton-Brown and Rahman, 2013). Both K27 and K36 are also the target of recurrent mutations in histone genes, leading to expression of so-called oncohistones (K27M and K36M), which are drivers of distinct types of pediatric cancers (Mohammad and Helin, 2017). Notably, K36 and K27 methylation landscapes are highly interdependent: when one modification is impaired, the other one increases and spreads (Lu et al., 2016; Oksuz et al., 2018; Stafford et al., 2018; Streubel et al., 2018). Consistent with this, a bi-directional antagonism was predicted based on computational modeling of *in vivo* K27 and K36 methylation dynamics measured by mass spectrometry in cancer cells (Zheng et al., 2012). Biochemical analysis showed that K36me2/3 directly blocked PRC2-mediated K27me2/3 on the same histone tail (Schmitges et al., 2011; Yuan et al., 2011), and deposition of K36me2 was proposed to directly limit K27me3 spreading (Streubel et al., 2018). Yet, genome-wide analysis showed substantial overlap between K27me2 and K36me2 and a moderate correlation between K27me3 and K36me2 (Streubel et al., 2018). Also, it remains unclear how K27me2/3 might counteract K36me2/3. Thus, the nature of the antagonistic relationship and how they may influence each other during maintenance and establishment remains puzzling.

In this study we take a quantitative approach to understand how histone modifications are inherited across cell division, monitoring *in vivo* dynamics of the tightly linked histone modifications K36me and K27me. We analyzed 15 distinct K27 and K36 methylation states on three different generations of histones. Using a mechanistic model for histone methylation, parameter inference, and quantitative hypothesis testing, we found that domains with distinct end-point methylation states had to be introduced to fit our data. We provide a detailed, quantitative picture of the K27me/K36me antagonistic relationship and reveal that co-occupancy of these modifications can be explained by their distinct establishment kinetics. We also demonstrate, using an EZH2 inhibitor, that the rate of *de novo* K27me3 on newly deposited histones is enhanced by pre-existing K27me3, lending strong support to the read-write model.

## RESULTS

### Slow K27me3 Establishment in Mouse ESCs (mESCs)

To identify the principles for how K27me and K36me patterns are propagated in mESCs, we chose a quantitative approach to measure how methylations developed over time on subsequent generations of histones (Figure 1A). We used triple stable isotope labeling by amino acids in cell culture (SILAC) with light (R0K0), medium (R6K4), and heavy (R10K8) amino acids to quantitate methylation patterns over time (Figures 1B and S1A). This scheme allowed us to measure methylation levels as they developed over time on pre-existing histones (generation 1), new histones incorporated in a narrow time window and allowed to age (generation 2), and new histones continuously incorporated over time to reach steady-state levels (generation 3) (Figure 1B).

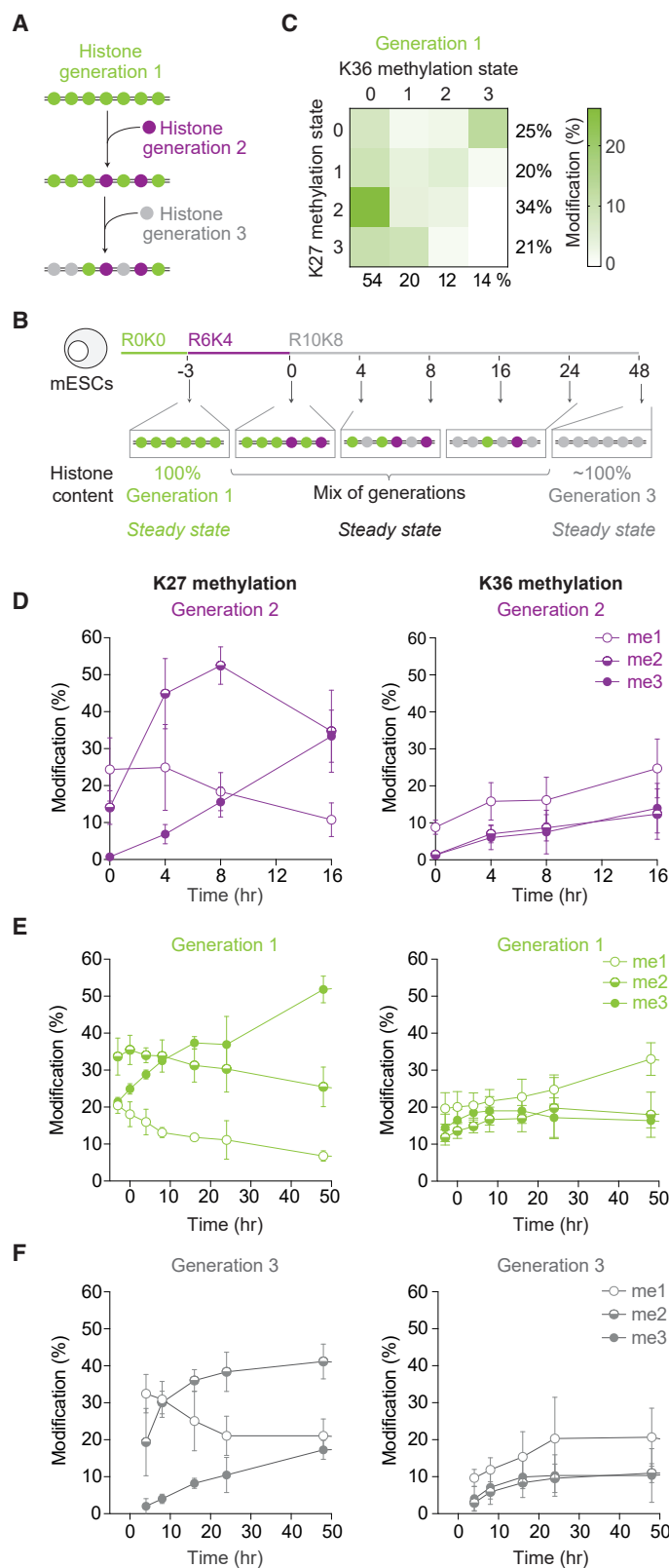


**Figure 1. Propagation Dynamics of K27 and K36 Methylation in mESCs**

(A) Strategy to analyze three successive histone generations by triple SILAC.

(B) Experimental design of pulse chase SILAC labeling in asynchronous mESCs.

(C) Heatmap showing the distribution of K27 and K36 methylation states in steady state prior to labeling. The sum of each methylation is shown on the right for K27 and at the bottom for K36.

(D) Methylation levels on generation 2 histones for K27 and K36. me1, mono-methyl; me2, di-methyl; me3, tri-methyl. Data are shown as mean  $\pm$  SD,  $n \geq 6$ .

(E) Methylation levels on generation 3 histones for K27 and K36. Data are shown as mean  $\pm$  SD,  $n \geq 6$ .

(F) Methylation levels on generation 1 histones for K27 and K36. Data are shown as mean  $\pm$  SD,  $n \geq 6$ .

See also Figure S1.



Before switching culture medium (Figure 1B,  $t = -3$  h), generation 1 histones constituted the total pool of nucleosomal histones and thus provided the total methylation level at steady state, including fully modified histones and histones that still underwent modification. We focused our analysis on combinatorial K27 and K36 methylation patterns and, for comparison, included analysis of H3K9 and H4K20 methylation. In steady state, the most abundant modification was K27me2 present on  $34\% \pm 5\%$  (mean  $\pm$  SD,  $n = 6$  experiments) of histone H3, while  $20\% \pm 2\%$  carried K27me1 and  $21\% \pm 1\%$  carried K27me3 (Figures 1C and S1B). About 50% of histones carried K36 methylation with K36me1 on  $20\% \pm 4\%$ , K36me2 on  $12\% \pm 2\%$ , and K36me3 on  $14\% \pm 4\%$ . This is overall in good accordance with previous mass spectrometry analysis of H3 methylation in mESCs growing in 2i medium (Lee et al., 2018; Oksuz et al., 2018).

We took advantage of the triple SILAC set-up to determine how K27 methylation is established on newly synthesized histones in generation 2. We observed a stepwise acquisition of K27 methylation (Figures 1D and S1C). K27me1 occurred almost concomitant with histone incorporation and reached its maximum at the 0-hour time point. This was followed by a surge of K27me2 within the first 3 h and a peak 8 h after incorporation. K27me3 establishment occurred with a substantial delay and continued to rise for more than 16 h after incorporation (Figure 1D). Consistent with the latter, the analysis of generation 1 histones demonstrated that old histones continued to gain K27me3 and progressed toward a higher methylation state (Figure 1E). As expected, generation 3 histones followed a trajectory toward the steady-state levels (Figure 1F), reaching methylation levels comparable to those of generation 1 at the beginning of the experiment (Figure S1B). Collectively, this mirrors the pattern of K27 methylation establishment in HeLa cells (Alabert et al., 2015), although the kinetics are faster in mESCs, matching their short cell cycle of around 15 h (Figure S1A). The continuous methylation on old histones is specific to K27, as neither K36me3 nor H3K9me3 continues to rise on old histones beyond one cell cycle (Figures 1F and S1E). This may reflect an inherent feature of the EZH2 enzyme that has a slow methylation rate for K27me2 to K27me3 (Justin et al., 2016; McCabe et al., 2012) and that the enzyme is challenged by the large substrate pool (in steady-state almost 75% of nucleosomal histones carry either K27me1/2/3) (Figures 1F and S1B). mESCs contain high concentration of PRC2 (Stafford et al., 2018) probably explaining how they maintain high levels of K27me3 level through rounds of rapid cell divisions despite slow K27 tri-methylation establishment (Figure S1B).

K36me1/2/3 establishment was continuous and slow, lasting from the time of incorporation up to 16 h, with K36me1 initiating shortly after incorporation and K36me2/3 delayed for a couple of hours (Figure 1D). K36me1 and K36me2 establishment were both delayed compared to K27me1 and K27me2, respectively. These kinetics largely agree with a previous study (Zheng et al., 2012). We observed a similar acquisition pattern for K9me1/2/3 (Figure S1E), while H4K20me1/2 showed stepwise acquisition similar to K27me1/2/3 (Figure S1F). It is not clear what governs this behavior, but it is notable that both K27me and H4K20me are highly abundant marks in mESCs 2i and

that K9me shows stepwise acquisition in HeLa cells, where K9me2/3 levels are much higher than in mESCs 2i (Alabert et al., 2015). Curiously, the K36me2 and K36me3 kinetics were highly similar, suggesting that K36me2, mediated by NSD1-3 and ASH1 enzymes, might be rate limiting for K36me3 establishment, mediated by SETD2. The division of labor between the enzymes that carry out di- and tri-methylation may thus be an obstacle for K36 tri-methylation.

### Computational Model for Propagation of K27 and K36 Methylation

Our approach allowed us to measure all combinatorial methylation states of K27 and K36 (Figure 1C) apart from K27me3K36me3, which was below our detection limit. To understand the dynamics in the three histone generations, we employed mechanistic modeling. Such a model can describe the temporal evolution of the methylation levels. By fitting mechanistic models to our comprehensive data, we were able to test hypotheses on global demethylation (Reveron-Gomez et al., 2018; Zheng et al., 2012) and the previously reported negative interaction between methylations on the two residues (Schmitges et al., 2011; Stafford et al., 2018; Voigt et al., 2012; Yuan et al., 2011). For a mathematical description, we used a system of ordinary differential equations and assumed that transitions between modifications followed mass action kinetics (see STAR Methods and Figures S2A and S2B for more details on the modeling). Moreover, newly incorporated histones during cell division were assumed to be unmodified on K27 and K36 (Alabert et al., 2015; Jasencakova et al., 2010; Loyola et al., 2006). Based on these assumptions, we considered two different model variants. In the “global model” (similar to the approach of Zheng et al., 2012; see STAR Methods for a detailed description and comparison), each state develops in time due to methylation and demethylation (Figure 2A). Here, each histone tail has the same rate to acquire or lose a methyl group, independent of its genomic position. Since the existence of global demethylation of histones has been questioned recently (Reveron-Gomez et al., 2018), we tested whether the global model required demethylation. We found that this model was not able to fit the data without accounting for demethylation (Figure 2C). Thus, we considered an alternative model without demethylation. This “domain” model was motivated by the idea that the genomic context of the histones might define its methylation state. It assumes that histones in certain domains can only be methylated up to a defined final state (Figure 2B). Domains may form due to constraints in the availability and activity of enzymes, reflecting that they are recruited and activated at specific regions of the genome (Ferrari et al., 2014; Lee et al., 2018) and lead to inhomogeneous distributions of enzymes in the nucleus. The domain to which a histone belongs dictates the final methylation state, i.e., whether it can be further methylated or not. Fitting the models to the data, we found that a domain model with 32 parameters and no demethylation (Figure 2B; STAR Methods) could explain modification dynamics in all generations similarly well as the global model with 30 parameters and active demethylation (Figures 2C and S2C–S2E; STAR Methods).

To examine the existence of global demethylation as the testable difference of the two model hypotheses, we inhibited K27

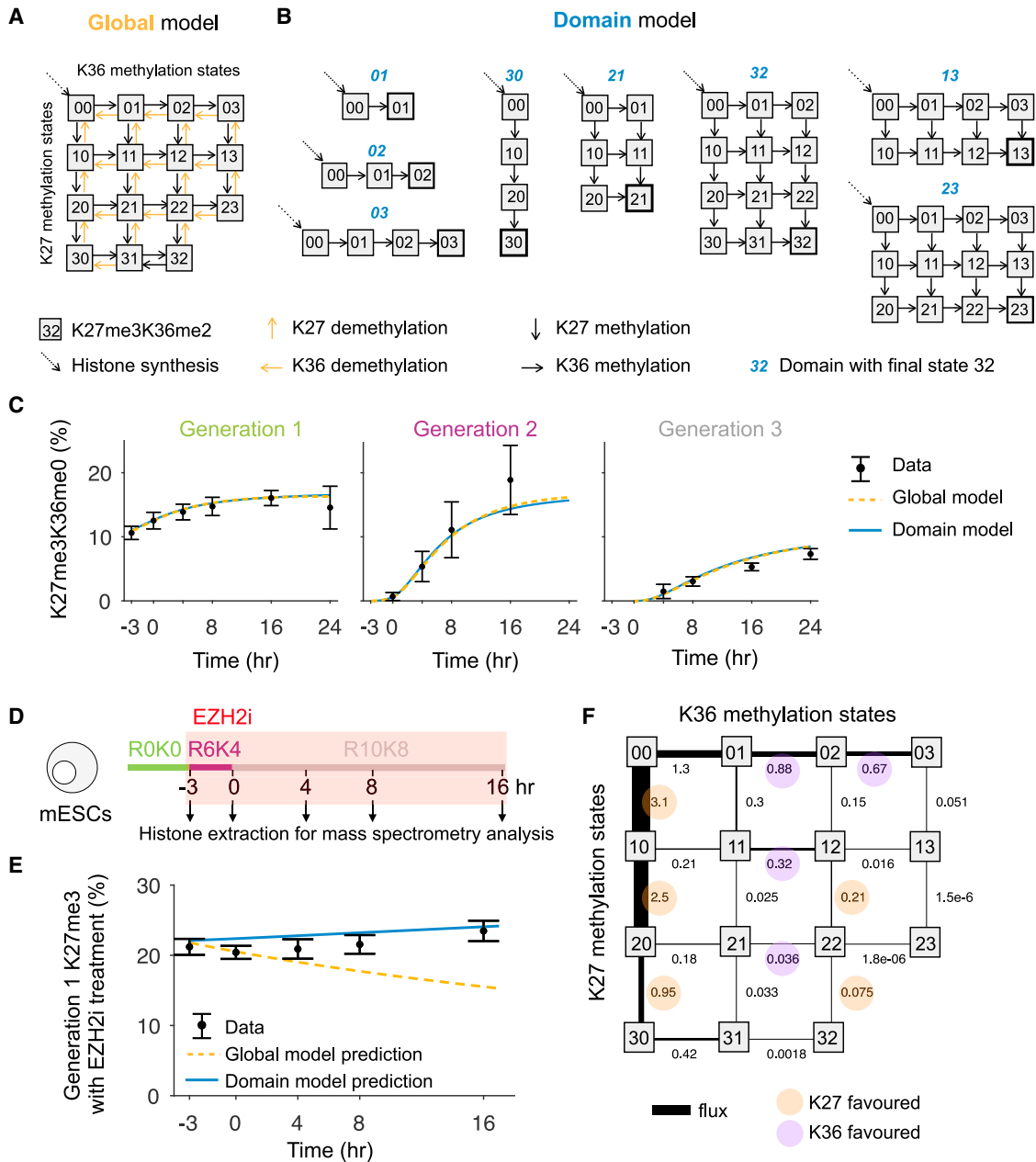


**Figure 2. Computational Domain Model Predicts Dynamics during Inhibitor Treatment without Global Demethylation**

(A) The global model describes the abundance of methylations on K27 and K36 with methylation and demethylation. Differences between generations occur from the incorporation of unmodified histones (dotted diagonal arrow): this only occurs for the time when the cells are in the corresponding culture medium.

(B) The domain model assumes that the histone tails are methylated until they reach a defined final state, which depends on the domain the histone belongs to. In contrast to the global model, it requires no demethylation.

(C) Both the global and domain model can describe methylation dynamics of untreated cells in all three generations. Data are shown as mean  $\pm$  SD,  $n = 9$ .

(D) Experimental design of EZH2i inhibitor treatment.

(E) Only the domain model prediction fits the K27me3 levels of generation 1 during inhibitor treatment. Data are shown as mean  $\pm$  SD,  $n = 3$ .

(F) The model averaged fluxes for the population steady state show antagonism between K27 and K36 methylation. The width of the black lines indicates the size of the flux.

See also Figure S2.

methylation with an EZH2 inhibitor (EPZ-6438) and measured the histone modification dynamics over time (Figure 2D). K27me3 levels remained stable at around 20% for 16 h (Figure 2E). We used this finding to test the two models. First, we estimate the efficiency of the EZH2 inhibitor from the ratio of K27me3 to K27me2 in untreated and treated cells to be around  $92.8\% \pm 5.2\%$  (mean  $\pm$  SD,  $n = 3$  replicates; see Figures S2F and S2G and STAR Methods for details). We then predicted K27me3 levels upon inhibitor treatment for the two model hypotheses. The experimentally observed stability of K27me3 in the presence of the inhibitor was inconsistent with the global model that assumed demethylation, but it could be well explained quantitatively with our domain model (Figure 2E). We thus rejected the global model and used the domain model to analyze our data further. The global model relies on substantial demethylation, with the differential activity of demethylases having to play a major role in establishing distinct methylated domains. In contrast, the domain model stresses the importance of the environment where the histones are deposited, with the differential activity of histone writers determining the final state. We note that the latter is consistent with recent literature showing that PRC2 accessory components, like JARID2 and PCLs, promote occupancy in K27me3 domains (e.g., CpG islands), while PRC2, devoid of such accessory factors, can reside in other genomic locations and promote H3K27me1/2 (Healy et al., 2019; Højfeldt et al., 2019; Schuettengruber et al., 2017).

To interrogate interactions between the two residues, we calculated the methylation flux in steady state, defined as the product of the modification state abundance times the reaction rate constant (STAR Methods). The fluxes from K27me0 to K27me3 with no K36 methylation made up 57.4% of all fluxes (Figure 2F). We found evidence for antagonistic behavior in both directions. In all cases with fluxes over  $0.5 \text{ h}^{-1}$ , the addition of a methyl mark to the site with the higher modified state was more likely than modification of the less modified site (Figures 2F and S2H). For example, there is a  $2.5/0.21 = 11.9$ -fold increased probability for further methylation of K27 on a histone already carrying K27me1K36me0 as compared to methylation of K36 and a  $0.67/0.15 = 4.5$ -fold increase for further methylation of K36 on K27me0K36me2 as compared to adding methylation to K27 (STAR Methods). In cases where the lysines are equally methylated, K27 methylation is favored on naive histones (K27me0K36me0) and on di-methylated histones (K27me2K36me2), while K36 methylation is favored when both residues are mono-methylated (K27me1K36me1). Collectively, our modeling provides a detailed quantitative picture of the antagonistic relationship between K27me and K36me. We previously proposed that an increased rate of cell division might lead to loss of K27me3 by dilution (Alabert et al., 2015) due to the slow rate of establishment on new histones. We tested this hypothesis by increasing the proliferation rate in our model, and this revealed that a shorter cell cycle (with all other parameters unchanged) will indeed reduce the steady-state level of K27me3 (Figure S2I). This is consistent with recent work showing that mESCs have higher levels of K27me3 when grown in 2i medium as compared to serum and leukemia inhibitory factor (LIF), which speeds up the cell cycle substantially (van Mierlo et al., 2019).

### Pre-existing K27me3 on Old Histones Increases the Rate of De Novo K27me3

Based on the ability of K27me3 to allosterically activate PRC2, it has been predicted that parental histones carrying K27me3 directly stimulate K27me3 establishment on newly incorporated histones (Margueron et al., 2009; Sanulli et al., 2015). Our quantitative system yielded the unique opportunity to test this hypothesis by directly measuring the contribution of parental K27me3 to K27me3 establishment on new histones (Figure 3A). To erase K27me3 from parental histones, cells were treated for 7 days with the EZH2 inhibitor (Figure 3B) (Højfeldt et al., 2018). After inhibitor treatment, the level of K27me3 dropped below 3% and K27me2 was also strongly reduced, while K27me1 accumulated (Figure 3C). This is consistent with previous work (Højfeldt et al., 2018) and suggests that, in this setting, EZH1, which is not targeted by the inhibitor, catalyzes K27me1. Focusing on the methylation kinetics on new histones (generation 2), we found that the establishment of K27me2/3 methylation was delayed in cells lacking K27me3 (Figure 3D). Establishment of other methylation marks, including H3K9me3 (Figure S3A), was not affected, excluding unspecific effects on methylation dynamics. We performed quantitative model selection to identify rate constants that differ between generation 2 histones of untreated and recovering cells (Figures 3E and S3B; STAR Methods). We found that a model with substantial differences in K27 mono-methylation of K27me0K36me0, K27 tri-methylation of K27me2K36me0, and K36 mono-methylation of K27me0K36me0 and K27me2K36me0 is able to explain the data and the differences between untreated and recovering cells (Figures 3E and S3B). The reduced rate of K27 mono-methylation of K27me0K36me0 and K27 tri-methylation of K27me2K36me0 strongly support the existence of a feed-forward loop, whereby parental K27me3 stimulates establishment of K27 methylation on new histones by increasing the enzymatic rate. The changes in K36 mono-methylation rates were unexpected, showing both up and downregulation. In particular, the 10-fold increased rate of K36 mono-methylation on K27me2K36me0 is substantial and further highlights the close interdependence of the K27 and K36 landscapes, as explored below.

### K36 Methylation Can Lock Cells in an Aberrant Modification State

Cells fully restored K27me3 levels after removal of the inhibitor within approximately five generations (Figure S3C), as reported previously (Højfeldt et al., 2018). This relatively slow recovery was unlikely to only reflect the delay in K27me2/3 on new histones, manifested on a scale of hours rather than cell generations. We thus also analyzed the recovery of the old histones (generation 1) after inhibitor treatment, expecting them to rapidly gain K27me3. Surprisingly, a large proportion of generation 1 histones were refractory to K27me3 after inhibitor removal, as compared to new generation 2 histones present in the same cells (Figure 4A). This result was counterintuitive given that a substantial fraction of generation 1 histones already carried K27me1 at the time of inhibitor removal (Figure 3C), and we thus sought to identify the basis for this recovery defect.

In-depth analysis of generation 1 histones revealed that there was a strong skew toward more K36me1/2 after inhibitor

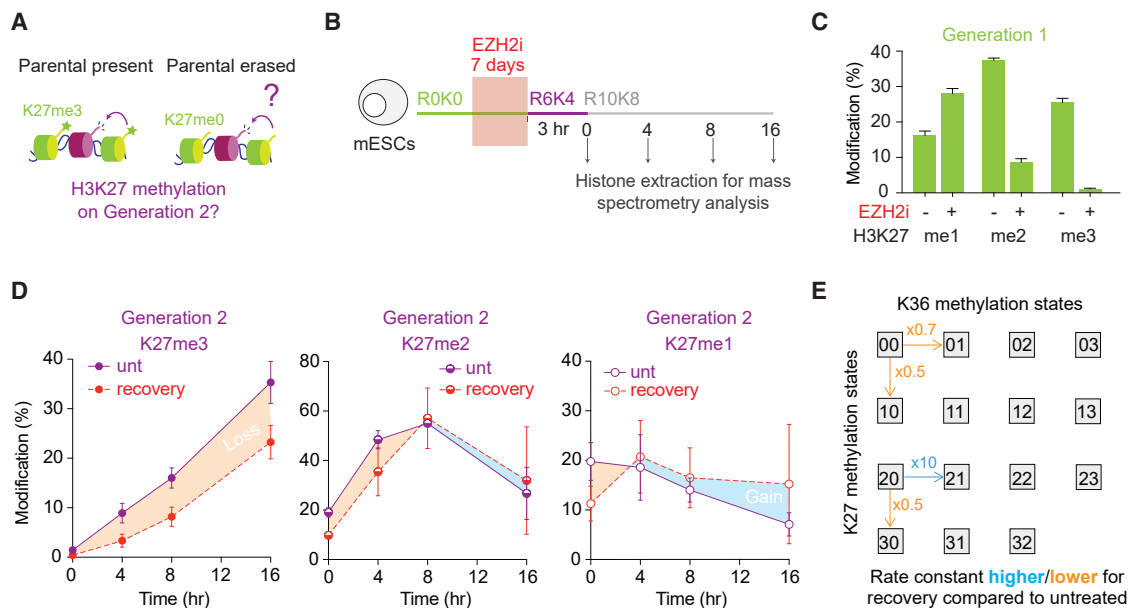


**Figure 3. Lack of K27me3 on Parental Histones Reduces the Rate of De Novo K27me3**

(A) Illustration of the question: do pre-existing K27me3 affect the kinetics of *de novo* K27me3 establishment?

(B) Experimental design to track *de novo* K27 methylation on generation 2 histones upon recovery from 7 days of EZH2 inhibitor treatment.

(C) K27 methylation levels on generation 1 histones after 7 days of EZH2 inhibitor treatment (measured at time 0 in B). Data are shown as mean  $\pm$  SD,  $n = 3$ .

(D) K27 methylation dynamics on generation 2 histones with losses and gains in the absence of pre-existing K27me3 highlighted by orange and blue shaded areas, respectively. Data are shown as mean  $\pm$  SD,  $n = 3$ .

(E) The domain model predicts differences in the rate constants between untreated and recovering generation 2 histones.

See also Figure S3.

treatment (Figure 4B) as well as a moderate loss of K36me3. This is consistent with recent findings in EED knockout mESCs, where loss of K27 methylation led to a 3-fold increase in K36me2 and reduction of K36me3 (Oksuz et al., 2018). Similar effects on K36me were observed upon genetic inhibition of PRC2 by expression of H3K27M (Figures S4A and S4B), excluding that K36 methylation changes were due to unspecific activity of the EZH2 inhibitor. Remarkably, our setup showed that the strong positive K36me1/2 skew was maintained throughout the lifetime of these histones, regardless of whether the EZH2 inhibitor was removed (Figure 4C, generation 1).

K36me2/3 inhibited PRC2-mediated K27me2/3 *in vitro* (Schmitges et al., 2011; Yuan et al., 2011), and modeling analysis (Figure 2F and Zheng et al., 2012) indicated that K36 methylation directly antagonizes K27 methylation. Taken together, this argues that K27me3 establishment on generation 1 histones is impaired because aberrant K36me2 inhibits PRC2 activity in *cis*. To further substantiate this hypothesis, we determined K36me2 occupancy across the genome by quantitative chromatin immunoprecipitation sequencing (ChIP-seq) analysis. Consistent with previous work (Streubel et al., 2018), K36me2 is a widespread mark in mESCs found in intergenic regions and across gene bodies (Figures 4D and S4F) and overlapping with all K27 methylation states (me1/2/3) (Figure S4G). Upon EZH2 inhibition, K36me2 levels increased genome wide, including genic and intergenic regions (Figures 4E and S4F). The increase in K36me2 was most prominent in K27me3 domains, in particular, those normally low in K36me2 (Fig-

ure S4H) as compared to regions marked by K27me1/2 (Figures 4F and 4G). Collectively, these results explain why K27me3 is impaired on generation 1 histones and reveals a surprising tardiness in reshaping the methylation landscape once established. Pre-existing K36 methylation makes cells refractory to change, allowing full recovery of K27me3 levels only after dilution of these pre-existing histones over 5 rounds of cell division. This underscores the importance of establishing correct histone modification patterns on new histones, as an unwarranted K36/K27 skew can affect cells across several cell divisions. Indeed, histones incorporated after removal of the inhibitor (generations 2 and 3) also showed reminiscence of the inhibitor-induced K36 methylation skew (Figures 4C and S4C–S4E). This is partly explained by the 10-fold elevated rate of K36 mono-methylation of K27me2K36me0 peptides (Figure 3E). Aberrant K36me2 on parental histones thus impacted subsequent generations of histones that did not experience the inhibitor treatment, further underscoring that acquisition of modifications on new histones is influenced by the environment where they land.

## DISCUSSION

Understanding how histone-based information is propagated across cell division remains a major challenge in biology. Here we take a quantitative modeling-based approach to tackle this question. By measuring K27 and K36 methylation dynamics on distinct histones, we developed a computational model that is reusable and provides a new analysis framework to understand

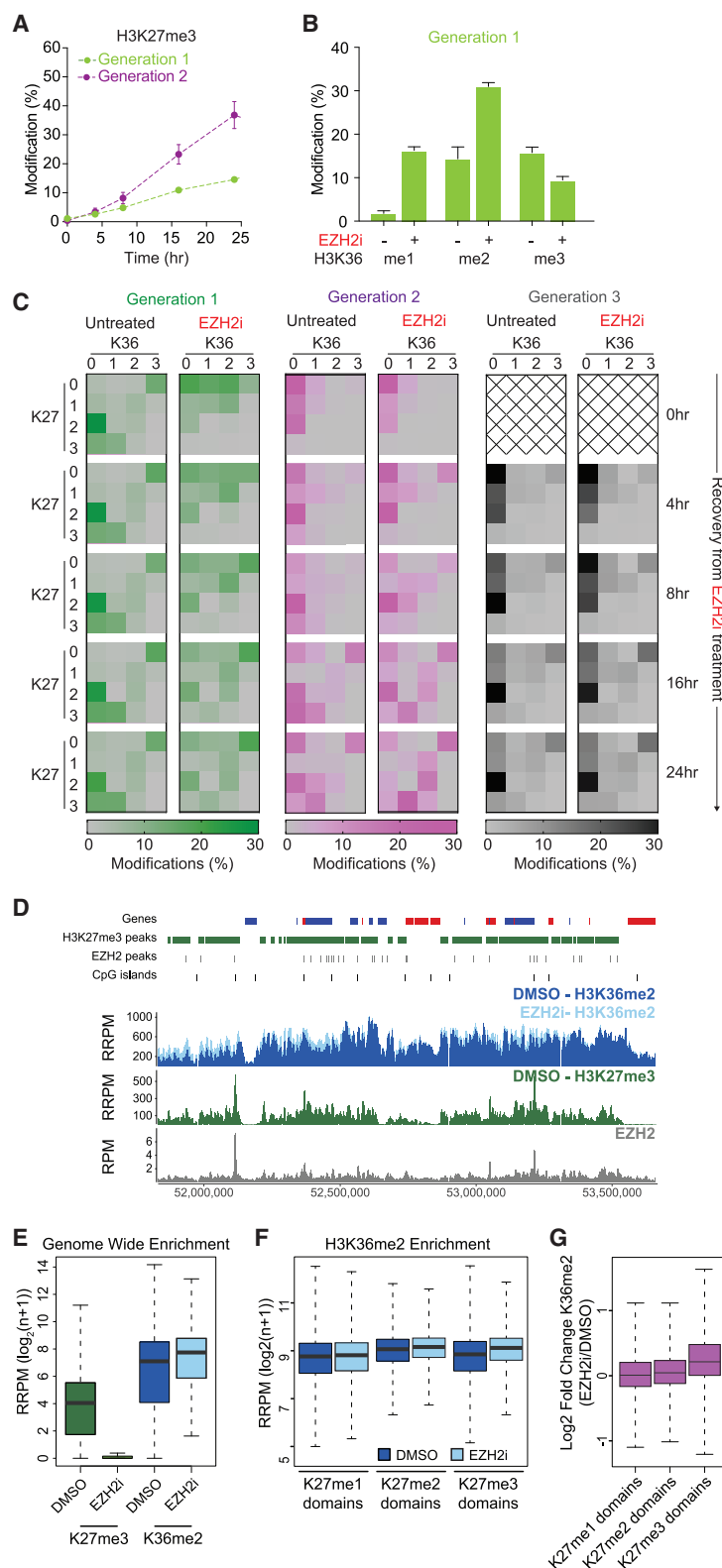


**Figure 4. K36 Methylation Locks Polycomb Domains in an Aberrant Modification State**

(A) K27me3 levels on generation 1 and generation 2 histones during recovery from EZH2 inhibitor treatment as described in Figure 3B. Data are shown as mean  $\pm$  SD,  $n = 3$ .

(B) K36 methylation levels on generation 1 histones after 7 days of EZH2 inhibitor treatment (time 0 in Figure 3B). Data are shown as mean  $\pm$  SD,  $n = 3$ .

(C) Heatmaps of K27 and K36 methylation levels on generation 1, 2, and 3 histones during recovery from inhibitor treatment described in Figure 3B.

(D) Screenshot of H3K36me2 ChIP-seq signal in DMSO- (dark blue) or EZH2i- (light blue) treated samples and H3K27me3 ChIP-seq signal in DMSO-treated samples (green). Quantitated with reference-adjusted reads per million (RRPM),  $\log_2(n + 1)$  over the region depicted. Bottom panel, EZH2 ChIP-seq signal (gray) from Marks et al. (2012) quantitated with reads per million (RPM) over the region depicted. Red and blue blocks represent genes in the forward or reverse strand, respectively. Green boxes indicate H3K27me3 peaks in untreated conditions. EZH2 peaks are depicted in gray and CpG islands in black.

(E) Left, boxplot of H3K36me2 and H3K27me3 ChIP-seq signal over 1 kb windows across the genome in DMSO- and EZH2i-treated samples. Black line, median; dashed lines,  $1.5 \times$  interquartile range. Quantitated with RRPm,  $\log_2(n + 1)$ .

(F) Boxplot of H3K36me2 ChIP-seq signal over 1 kb windows across H3K27me1, H3K27me2, and H3K27me3 domains. Black line, median; dashed lines,  $1.5 \times$  interquartile range. Quantitated with RRPm,  $\log_2(n + 1)$ .

(G) Boxplot of log2 fold change of H3K36me2 signal in EZH2i-treated samples as compared to DMSO-treated samples in H3K27me1, H3K27me2, and H3K27me3 domains.

See also Figure S4.



propagation of histone modifications. Our data-driven model selection rejects global K27 and K36 demethylation, provides *in vivo* rate constants for individual reactions, and argues for the existence of distinct methylation domains. By studying recovery from EZH2 inhibition, we found that pre-existing K27me3 on old histones stimulated the rate of *de novo* K27me3 establishment. Our model also revealed a detailed, quantitative picture of the mutual antagonism between K27 and K36 methylation states. Consistent with this, inhibition of EZH2 reshapes the K36me landscape, which in turn stabilizes the aberrant state and impedes restoration of K27me3 upon inhibitor removal.

Our modeling approach was inspired by the model of Zheng et al. (2012). Indeed, the global model (Figure 2A) has the same model structure as presented in Zheng et al. (2012), although we omitted 22 individual demethylation rates in favor of three demethylation rates for K27 and three for K36 to avoid overfitting. However, a model with demethylation cannot explain stable K27me3 states during inhibitor treatment: if K27me2 sites are no longer methylated, demethylation should lead to a clear decrease of K27me3 over time. We thus introduce a domain model (Figure 2B) that is able to explain our data and is consistent with no global demethylation (Reveron-Gomez et al., 2018). Our domain model argues for the existence of distinct populations of histones that progress toward specific states. This is consistent with well-established principles of chromatin organization where specific post-translational modifications occupy distinct genomic locations (CpG islands, gene bodies, promoter regions) and even form discrete 3D structures in the cell nucleus (Polycomb bodies). Thus, histones are not equal in their methylation potential, but their site of incorporation is decisive for the methylation state they will acquire. Similar to Zheng et al. (2012), we found antagonism between K27 and K36 methylation. While Zheng et al. (2012) argue that this antagonism manifests in decreasing K36 methylation rate constants with increasing K27 methylations (and vice versa), we believe that a direct comparison of K27 and K36 methylation fluxes for a particular state is more appropriate. Indeed, once either K27 or K36 is set on an otherwise balanced histone, the addition of more methylation marks of the same kind is often more likely for high-flux states (Figure 2F). Such a “the rich get richer” analogy seems to be particularly relevant for understating the recovery from inhibition. There, histones that have traversed to a high K36 methylation state upon K27 inhibition are no longer able to regain untreated K27 levels, probably because they are stuck in a particular domain. Similar to other models that describe epigenetic modifications in a quantitative manner (Berry et al., 2017; Blasi et al., 2016), we also assumed mass action kinetics for transitions between chromatin states. In contrast to other approaches, however, we explicitly fit combinatorial histone dynamics in a variety of experimental settings. This allowed us to infer structure and kinetics in an unprecedented manner.

The intriguing read-write function of the enzymes that catalyze key repressive histone modifications like K27me3 and H3K9me3 argues that chromatin states are maintained across cell division through self-propagation (Reinberg and Vales, 2018). For PRC2, this read-write mechanism involves the recognition of K27me3 by an aromatic cage in the EED subunit, which in turn leads to

allosteric activation of EZH2 (Reinberg and Vales, 2018). Structural data support that the read-write mechanism operates between neighboring nucleosomes (Poepsel et al., 2018), which is relevant after replication, where nucleosomes are assembled from either modified parental histone H3-H4 tetramers or new unmodified H3-H4 (Xu et al., 2010). However, the biological significance of the read-write mechanism remains a matter of debate. Self-propagation alone is not sufficient for K27me3 maintenance in *Drosophila*, as a genetic contribution from polycomb response elements (PREs) is also required (Coleman and Struhl, 2017; Laprell et al., 2017). Establishment of the K27me3 landscape in mESCs can also occur in the absence of pre-existing K27me3 (Højfeldt et al., 2018; Oksuz et al., 2018) and in EED allosteric activation mutants (Oksuz et al., 2018). However, EED allosteric activation mutants are delayed in K27 methylation and fail to re-establish wild-type levels of K27me3 (Oksuz et al., 2018), arguing for the importance of the read-write mechanism in K27me3 maintenance. However, PRC2 also methylates its binding partner JARID2 on a K27 mimicking peptide that can activate the enzyme allosterically (Sanulli et al., 2015), and this might contribute to reduced activity of the EED mutants. By measuring methylation on new histones specifically, we showed that the lack of pre-existing K27me3 reduced the efficiency of *de novo* K27me3 establishment. Using mathematical modeling, we can assign this in part to a reduced rate of K27 methylation. This demonstrates that pre-existing H3K27me3 stimulates *de novo* K27 methylation during DNA replication and argues that self-propagation through a read-write mechanism is important for timely restoration of K27me3 domains.

Our model shows a complex pattern of mutual antagonism between methylation on K27 and K36. This corroborates and extends a number of other *in vivo* and *in vitro* studies. *In vitro*, the presence of K36me2/3 reduces the activity of EZH2 mediated methylation in *cis*, while there are no reports that K27me2/3 directly impair the activity of K36me2/3 methyltransferases (Jani et al., 2019; Schmitges et al., 2011; Voigt et al., 2012; Yuan et al., 2011). Inhibition of K36 methylation, by expressing the H3K36M oncohistone in cancer cells or upon NSD1 deletion in ESCs, leads to aberrant gain and spreading of K27me3 (Lu et al., 2016; Streubel et al., 2018). Likewise, expression of the K27M oncohistone leads to increased levels of K36me2 and its aberrant spreading into K27me3 domains (Stafford et al., 2018; this paper). Our modeling shows a two-way antagonism that is more complex and broadly involves K27 and K36 methylation stages. However, there is currently no evidence to support a direct effect of K27 methylation on K36 methyltransferases, leading us to suggest that this antagonism reflects chromatin compaction or reduced affinity of the K36 methyltransferases in a K27me context. Consistent with this view, we found a remarkable increase in the rate of K36 mono-methylation on K27me2K36me0 (on new histones) when K27me2/3 was erased from pre-existing histones. Quantitative ChIP-seq analysis confirmed increased K36me2 upon EZH2 inhibition, but the effect was less dramatic than indicated by mass spectrometry analysis. Given that most nucleosomes show asymmetric K27me3 (Voigt et al., 2012), part of the K36me2 gain might reflect an increase in symmetric K36me that would be masked in ChIP-seq experiments. In cells,

K27me3 and K36me3 domains do not generally overlap, but there is a substantial overlap of the K36me2 signal with K27me2 occupancy as well as some overlap with K27me3 domains (this paper; Streubel et al., 2018). It was suggested that these modifications might occur on different nucleosomes. However, mass spectrometry analysis shows substantial co-occurrence of these marks on the same histone tail (K36me2-3K27me1/2/3: 11.6%) (this paper; Jung et al., 2010; Zheng et al., 2012), arguing that they are not mutually exclusive. Our modeling and kinetics analysis indicate that K27me is imposed first, followed by methylation of K36, as speculated previously (Schmitges et al., 2011). This explains how histone H3 can acquire both marks despite K36me directly impairing PRC2 activity. If K36me is allowed to establish first (as in the context of EZH2 inhibition), this in turn impairs K27me2/3 establishment on those nucleosomes.

We propose that one biological implication of the K27/K36 methylation antagonism is to enhance stability of epigenetic states. Methylation on these sites, in particular K36me2 and K27me3 (Streubel et al., 2018 and this paper), are keeping each other in check by restraining unwarranted spreading. We observed that, upon recovery from EZH2 inhibition, pre-existing histones did not acquire K27me3 and retained an aberrant high level of K36me2. The epigenetic state of old histones is thus locked, in this case, in an aberrant state, and changing this state during recovery relies on dilution by new naive histones during replication in order to reset the K27/K36 methylation balance. This resistance to change is further enhanced by the lack of EZH2 allosteric activation in early recovery (see above) and, intriguingly, a slight skew toward K36me for several histone generations. The prediction from these observations (and the fact that almost all histone tails carry some level of K27/K36 methylation) is that the K27/K36 methylation antagonism stabilizes epigenetic states and provides a barrier to changes in cell identity that can be overridden globally by cell proliferation. Recently, profiling histone modifications in tumor samples has revealed pervasive K27me3 loss and K36me2 gain across different cancers (Noborini et al., 2019). We provide evidence that an increased rate of cell division alone might lead to the loss of K27me3 by dilution (this paper; Alabert et al., 2015). In addition to mutations in histones and chromatin regulators that directly affect K27/K36 methylation balance, a more general reduction in K27me3 might thus be driven by changes in proliferation rates during cellular transformation. This is relevant to consider in the context of targeted therapeutic intervention aimed at resetting the epigenetic landscape.

## STAR★METHODS

Detailed methods are provided in the online version of this paper and include the following:

- KEY RESOURCE TABLE
- LEAD CONTACT AND MATERIALS AVAILABILITY
- EXPERIMENTAL MODEL AND SUBJECT DETAILS
  - E14 mESCs cell culture
  - *Drosophila* S2 Cell Culture
  - TIG3 K27M and TIG3K9M cell lines generation
  - TIG3 K27M and TIG3K9M cell culture

## ● METHOD DETAILS

- EZH2 inhibition and wash out
- Sample preparation for histone modification analysis by MS
- LC-MS analysis of histone modifications
- Quantification of histone modifications
- ChIP-seq
- Data sequencing, processing and analyses
- Peak calling
- Mathematical modeling of histone tail methylation
- Global model
- Domain model
- Model calibration
- Model reduction and averaging
- Model prediction and validation
- Modeling differences between generation 2 histones in untreated and recovery experiments
- Implementation

## ● QUANTIFICATION AND STATISTICAL ANALYSIS

## ● DATA AND CODE AVAILABILITY

## SUPPLEMENTAL INFORMATION

Supplemental Information can be found online at <https://doi.org/10.1016/j.celrep.2019.12.060>.

## ACKNOWLEDGMENTS

We thank Jonas Hojfeldt and the K. Helin laboratory for advice on mESCs and EZH2 inhibitor treatment and Kathleen Stewart-Morgan and members of the Groth, Imhof, and Marr laboratories for fruitful discussions. This work was supported by a collaborative grant from the Lundbeck Foundation, Denmark (R198-2015-269), to A.G., A.I., and C.M. Research in the Groth lab was additionally supported by the European Research Council, European Union (ERC CoG no. 724436), Independent Research Fund Denmark (7016-00042B), and the Novo Nordisk Foundation (NNF14CC0001). C.A. is supported by the European Research Council, European Union (ERC Stg no. 715127). L.S. was funded by the BMBF, Germany project TIDY (031L0170B).

## AUTHOR CONTRIBUTIONS

C.A. performed the cell work. M.V.-A. performed all mass spectrometric measurements and analyzed the data together with C.A., C.L., and A.I. I.F. assisted with mass spectrometry. C.L., J.H., and C.M. developed the models. C.L. developed and L.S. reviewed the code. C.L. wrote the modeling supplement with L.S., C.M., and J.H. N.R.-G. and S.G. performed ChIP-seq analysis. C.A. and A.G. wrote the manuscript with input from all authors.

## DECLARATION OF INTERESTS

A.G. is cofounder and CSO of Ankrin Therapeutics. A.I. and M.V.-A. are cofounders of EpiQMax.

Received: September 17, 2019

Revised: November 25, 2019

Accepted: December 16, 2019

Published: January 28, 2020

## REFERENCES

Alabert, C., Barth, T.K., Reverón-Gómez, N., Sidoli, S., Schmidt, A., Jensen, O.N., Imhof, A., and Groth, A. (2015). Two distinct modes for propagation of histone PTMs across the cell cycle. *Genes Dev.* 29, 585–590.

- Allshire, R.C., and Madhani, H.D. (2018). Ten principles of heterochromatin formation and function. *Nat. Rev. Mol. Cell Biol.* 19, 229–244.
- Berry, S., Dean, C., and Howard, M. (2017). Slow Chromatin Dynamics Allow Polycomb Target Genes to Filter Fluctuations in Transcription Factor Activity. *Cell Syst.* 4, 445–457.e8.
- Blackledge, N.P., Farcas, A.M., Kondo, T., King, H.W., McGouran, J.F., Hanssen, L.L., Ito, S., Cooper, S., Kondo, K., Koseki, Y., et al. (2014). Variant PRC1 complex-dependent H2A ubiquitylation drives PRC2 recruitment and polycomb domain formation. *Cell* 157, 1445–1459.
- Blasi, T., Feller, C., Feigelman, J., Hasenauer, J., Imhof, A., Theis, F.J., Becker, P.B., and Marr, C. (2016). Combinatorial Histone Acetylation Patterns Are Generated by Motif-Specific Reactions. *Cell Syst.* 2, 49–58.
- Coleman, R.T., and Struhl, G. (2017). Causal role for inheritance of H3K27me3 in maintaining the OFF state of a *Drosophila* HOX gene. *Science* 356, 356.
- ENCODE Project Consortium (2012). An integrated encyclopedia of DNA elements in the human genome. *Nature* 489, 57–74.
- Cooper, S., Dienstbier, M., Hassan, R., Schermelleh, L., Sharif, J., Blackledge, N.P., De Marco, V., Elderkin, S., Koseki, H., Klose, R., et al. (2014). Targeting polycomb to pericentric heterochromatin in embryonic stem cells reveals a role for H2AK119u1 in PRC2 recruitment. *Cell Rep.* 7, 1456–1470.
- Ernst, J., and Kellis, M. (2010). Discovery and characterization of chromatin states for systematic annotation of the human genome. *Nat. Biotechnol.* 28, 817–825.
- Ferrari, K.J., Scelfo, A., Jammula, S., Cuomo, A., Barozzi, I., Stützer, A., Fischle, W., Bonaldi, T., and Pasini, D. (2014). Polycomb-dependent H3K27me1 and H3K27me2 regulate active transcription and enhancer fidelity. *Mol. Cell* 53, 49–62.
- Fröhlich, F., Kaltenbacher, B., Theis, F.J., and Hasenauer, J. (2017). Scalable Parameter Estimation for Genome-Scale Biochemical Reaction Networks. *PLoS Comput. Biol.* 13, e1005331.
- Hass, H., Loos, C., Raimúndez-Álvarez, E., Timmer, J., Hasenauer, J., and Kreutz, C. (2019). Benchmark problems for dynamic modeling of intracellular processes. *Bioinformatics* 35, 3073–3082.
- Healy, E., Mucha, M., Glancy, E., Fitzpatrick, D.J., Conway, E., Neikes, H.K., Monger, C., Van Mierlo, G., Baltissen, M.P., Koseki, Y., et al. (2019). PRC2.1 and PRC2.2 Synergize to Coordinate H3K27 Trimethylation. *Mol. Cell* 76, 437–452.e6.
- Hindmarsh, A.C., Brown, P.N., Grant, K.E., Lee, S.L., Serban, R., Shumaker, D.E., and Woodward, C.S. (2005). SUNDIALS: Suite of Nonlinear and Differential/Algebraic Equation Solvers. *ACM Trans. Math. Softw.* 31, 363–396.
- Højfeldt, J.W., Laugesen, A., Willumsen, B.M., Damhofer, H., Hedehus, L., Tvardovskiy, A., Mohammad, F., Jensen, O.N., and Helin, K. (2018). Accurate H3K27 methylation can be established de novo by SUZ12-directed PRC2. *Nat. Struct. Mol. Biol.* 25, 225–232.
- Højfeldt, J.W., Hedehus, L., Laugesen, A., Tatar, T., Wiehle, L., and Helin, K. (2019). Non-core Subunits of the PRC2 Complex Are Collectively Required for Its Target-Site Specificity. *Mol. Cell* 76, 423–436.e3.
- Huang, C., and Zhu, B. (2018). Roles of H3K36-specific histone methyltransferases in transcription: antagonizing silencing and safeguarding transcription fidelity. *Biophys. Rep.* 4, 170–177.
- Jani, K.S., Jain, S.U., Ge, E.J., Diehl, K.L., Lundgren, S.M., Müller, M.M., Lewis, P.W., and Muir, T.W. (2019). Histone H3 tail binds a unique sensing pocket in EZH2 to activate the PRC2 methyltransferase. *Proc. Natl. Acad. Sci. USA* 116, 8295–8300.
- Jasencakova, Z., Scharf, A.N., Ask, K., Corpet, A., Imhof, A., Almouzni, G., and Groth, A. (2010). Replication stress interferes with histone recycling and predeposition marking of new histones. *Mol. Cell* 37, 736–743.
- Jung, H.R., Pasini, D., Helin, K., and Jensen, O.N. (2010). Quantitative mass spectrometry of histones H3.2 and H3.3 in Suz12-deficient mouse embryonic stem cells reveals distinct, dynamic post-translational modifications at Lys-27 and Lys-36. *Mol. Cell. Proteomics* 9, 838–850.
- Justin, N., Zhang, Y., Tarricone, C., Martin, S.R., Chen, S., Underwood, E., De Marco, V., Haire, L.F., Walker, P.A., Reinberg, D., et al. (2016). Structural basis of oncogenic histone H3K27M inhibition of human polycomb repressive complex 2. *Nat. Commun.* 7, 11316.
- King, H.W., Fursova, N.A., Blackledge, N.P., and Klose, R.J. (2018). Polycomb repressive complex 1 shapes the nucleosome landscape but not accessibility at target genes. *Genome Res.* 28, 1494–1507.
- Langmead, B., and Salzberg, S.L. (2012). Fast gapped-read alignment with Bowtie 2. *Nat. Methods* 9, 357–359.
- Laprell, F., Finkl, K., and Müller, J. (2017). Propagation of Polycomb-repressed chromatin requires sequence-specific recruitment to DNA. *Science* 356, 85–88.
- Laugesen, A., Højfeldt, J.W., and Helin, K. (2019). Molecular Mechanisms Directing PRC2 Recruitment and H3K27 Methylation. *Mol. Cell* 74, 8–18.
- Lee, C.H., Yu, J.R., Kumar, S., Jin, Y., LeRoy, G., Bhanu, N., Kaneko, S., Garcia, B.A., Hamilton, A.D., and Reinberg, D. (2018). Allosteric Activation Dictates PRC2 Activity Independent of Its Recruitment to Chromatin. *Mol. Cell* 70, 422–434.e6.
- Loos, C., Krause, S., and Hasenauer, J. (2018). Hierarchical optimization for the efficient parametrization of ODE models. *Bioinformatics* 34, 4266–4273.
- Loyola, A., Bonaldi, T., Roche, D., Imhof, A., and Almouzni, G. (2006). PTMs on H3 variants before chromatin assembly potentiate their final epigenetic state. *Mol. Cell* 24, 309–316.
- Lu, C., Jain, S.U., Hoelper, D., Bechet, D., Molden, R.C., Ran, L., Murphy, D., Venneti, S., Hameed, M., Pawel, B.R., et al. (2016). Histone H3K36 mutations promote sarcomagenesis through altered histone methylation landscape. *Science* 352, 844–849.
- MacLean, B., Tomazela, D.M., Shulman, N., Chambers, M., Finney, G.L., Freuden, B., Kern, R., Tabb, D.L., Liebler, D.C., and MacCoss, M.J. (2010). Skyline: an open source document editor for creating and analyzing targeted proteomics experiments. *Bioinformatics* 26, 966–968.
- Maier, C., Loos, C., and Hasenauer, J. (2017). Robust parameter estimation for dynamical systems from outlier-corrupted data. *Bioinformatics* 33, 718–725.
- Margueron, R., Justin, N., Ohno, K., Sharpe, M.L., Son, J., Drury, W.J., 3rd, Voigt, P., Martin, S.R., Taylor, W.R., De Marco, V., et al. (2009). Role of the polycomb protein EED in the propagation of repressive histone marks. *Nature* 461, 762–767.
- Marks, H., Kalkan, T., Menafra, R., Denissov, S., Jones, K., Hofemeister, H., Nichols, J., Kranz, A., Stewart, A.F., Smith, A., and Stunnenberg, H.G. (2012). The transcriptional and epigenomic foundations of ground state pluripotency. *Cell* 149, 590–604.
- McCabe, M.T., Graves, A.P., Ganji, G., Diaz, E., Halsey, W.S., Jiang, Y., Smitheman, K.N., Ott, H.M., Pappalardi, M.B., Allen, K.E., et al. (2012). Mutation of A677 in histone methyltransferase EZH2 in human B-cell lymphoma promotes hypertrimethylation of histone H3 on lysine 27 (H3K27). *Proc. Natl. Acad. Sci. USA* 109, 2989–2994.
- Mohammad, F., and Helin, K. (2017). Oncohistones: drivers of pediatric cancers. *Genes Dev.* 31, 2313–2324.
- Noberini, R., Restellini, C., Savoia, E.O., Raimondi, F., Ghiani, L., Jodice, M.G., Bertalot, G., Bonizzi, G., Capra, M., Maffini, F.A., et al. (2019). Profiling of Epigenetic Features in Clinical Samples Reveals Novel Widespread Changes in Cancer. *Cancers (Basel)* 11, 11.
- Oksuz, O., Narendra, V., Lee, C.H., Descostes, N., LeRoy, G., Raviram, R., Blumenberg, L., Karch, K., Rocha, P.P., Garcia, B.A., et al. (2018). Capturing the Onset of PRC2-Mediated Repressive Domain Formation. *Mol. Cell* 70, 1149–1162.e5.
- Petryk, N., Dalby, M., Wenger, A., Stromme, C.B., Strandsby, A., Andersson, R., and Groth, A. (2018). MCM2 promotes symmetric inheritance of modified histones during DNA replication. *Science* 361, 1389–1392.
- Poepsel, S., Kasinath, V., and Nogales, E. (2018). Cryo-EM structures of PRC2 simultaneously engaged with two functionally distinct nucleosomes. *Nat. Struct. Mol. Biol.* 25, 154–162.
- Reinberg, D., and Vales, L.D. (2018). Chromatin domains rich in inheritance. *Science* 361, 33–34.

- Reveron-Gomez, N., Gonzalez-Aguilera, C., Stewart-Morgan, K.R., Petryk, N., Flury, V., Graziano, S., Johansen, J.V., Jakobsen, J.S., Alabert, C., and Groth, A. (2018). Accurate Recycling of Parental Histones Reproduces the Histone Modification Landscape during DNA Replication. *Mol Cell* 72, 239–249.e5.
- Sanulli, S., Justin, N., Teissandier, A., Ancelin, K., Portoso, M., Caron, M., Michaud, A., Lombard, B., da Rocha, S.T., Offer, J., et al. (2015). Jarid2 Methylation via the PRC2 Complex Regulates H3K27me3 Deposition during Cell Differentiation. *Mol. Cell* 57, 769–783.
- Scharf, A.N., Barth, T.K., and Imhof, A. (2009). Establishment of histone modifications after chromatin assembly. *Nucleic Acids Res.* 37, 5032–5040.
- Schmitges, F.W., Prusty, A.B., Faty, M., Stützer, A., Lingaraju, G.M., Aiwazian, J., Sack, R., Hess, D., Li, L., Zhou, S., et al. (2011). Histone methylation by PRC2 is inhibited by active chromatin marks. *Mol. Cell* 42, 330–341.
- Schuettengruber, B., Bourbon, H.M., Di Croce, L., and Cavalli, G. (2017). Genome Regulation by Polycomb and Trithorax: 70 Years and Counting. *Cell* 171, 34–57.
- Schwarz, G. (1978). Estimating the dimension of a model. *Ann. Stat.* 6, 461–464.
- Stafford, J.M., Lee, C.H., Voigt, P., Descostes, N., Saldana-Meyer, R., Yu, J.R., Leroy, G., Oksuz, O., Chapman, J.R., Suarez, F., et al. (2018). Multiple modes of PRC2 inhibition elicit global chromatin alterations in H3K27M pediatric glioma. *Sci Adv.* 4, eaau5935.
- Stapor, P., Weindl, D., Ballnus, B., Hug, S., Loos, C., Fiedler, A., Krause, S., Hroß, S., Fröhlich, F., Hasenauer, J., and Wren, J. (2018). PESTO: Parameter ESTimation TOolbox. *Bioinformatics* 34, 705–707.
- Streubel, G., Watson, A., Jammula, S.G., Scelfo, A., Fitzpatrick, D.J., Oliviero, G., McCole, R., Conway, E., Glancy, E., Negri, G.L., et al. (2018). The H3K36me2 Methyltransferase Nsd1 Demarcates PRC2-Mediated H3K27me2 and H3K27me3 Domains in Embryonic Stem Cells. *Mol Cell* 70, 371–379.e5.
- Tatton-Brown, K., and Rahman, N. (2013). The NSD1 and EZH2 overgrowth genes, similarities and differences. *Am. J. Med. Genet. C. Semin. Med. Genet.* 163C, 86–91.
- van Mierlo, G., Dirks, R.A.M., De Clerck, L., Brinkman, A.B., Huth, M., Kloet, S.L., Saksouk, N., Kroeze, L.I., Willems, S., Farlik, M., et al. (2019). Integrative Proteomic Profiling Reveals PRC2-Dependent Epigenetic Crosstalk Maintains Ground-State Pluripotency. *Cell Stem Cell* 24, 123–137.e8.
- Voigt, P., LeRoy, G., Drury, W.J., 3rd, Zee, B.M., Son, J., Beck, D.B., Young, N.L., Garcia, B.A., and Reinberg, D. (2012). Asymmetrically modified nucleosomes. *Cell* 151, 181–193.
- Wasserman, L. (2000). Bayesian model selection and model averaging. *J. Math. Psychol.* 44, 92–107.
- Xu, M., Long, C., Chen, X., Huang, C., Chen, S., and Zhu, B. (2010). Partitioning of histone H3-H4 tetramers during DNA replication-dependent chromatin assembly. *Science* 328, 94–98.
- Xu, M., Chen, S., and Zhu, B. (2012). Investigating the cell cycle-associated dynamics of histone modifications using quantitative mass spectrometry. *Methods Enzymol.* 512, 29–55.
- Yu, C., Gan, H., Serra-Cardona, A., Zhang, L., Gan, S., Sharma, S., Johansson, E., Chabes, A., Xu, R.M., and Zhang, Z. (2018). A mechanism for preventing asymmetric histone segregation onto replicating DNA strands. *Science* 361, 1386–1389.
- Yu, J.R., Lee, C.H., Oksuz, O., Stafford, J.M., and Reinberg, D. (2019). PRC2 is high maintenance. *Genes Dev.* 33, 903–935.
- Yuan, W., Xu, M., Huang, C., Liu, N., Chen, S., and Zhu, B. (2011). H3K36 methylation antagonizes PRC2-mediated H3K27 methylation. *J. Biol. Chem.* 286, 7983–7989.
- Zang, C., Schones, D.E., Zeng, C., Cui, K., Zhao, K., and Peng, W. (2009). A clustering approach for identification of enriched domains from histone modification ChIP-Seq data. *Bioinformatics* 25, 1952–1958.
- Zheng, Y., Sweet, S.M., Popovic, R., Martinez-Garcia, E., Tipton, J.D., Thomas, P.M., Licht, J.D., and Kelleher, N.L. (2012). Total kinetic analysis reveals how combinatorial methylation patterns are established on lysines 27 and 36 of histone H3. *Proc. Natl. Acad. Sci. USA* 109, 13549–13554.

## STAR★METHODS

### KEY RESOURCE TABLE

REAGENT or RESOURCE	SOURCE	IDENTIFIER
<b>Antibodies</b>		
Bridging antibody	Active Motif	53017; RRID:AB_2793470
Mouse monoclonal anti H3K27me1	Active Motif	61015; RRID:AB_2715573
Rabbit monoclonal anti H3K27me2	Cell Signaling	9728; RRID:AB_1281338
Rabbit monoclonal anti H3K27me3	Cell Signaling	9733; RRID:AB_2616029
Rabbit monoclonal anti H3K36me2	AbCam	176921
Rabbit polyclonal anti H3K36me3	AbCam	9050; RRID:AB_306966
<b>Chemicals, Peptides, and Recombinant Proteins</b>		
EZH2 inhibitor	MedChem Express	EPZ6438
Shields and Sang M3 insect medium	Sigma-Aldrich	Cat No. S8398
Protein A-Sepharose® 4B, Fast Flow from Staphylococcus aureus	Sigma-Aldrich	Cat No. P9424-1ML
Protein G Sepharose®, Fast Flow	Sigma-Aldrich	Cat No. P3296-1ml
Agencourt AMPure XP	Beckman Coulter	Cat No. A63880
<b>Critical Commercial Assays</b>		
truChIP Chromatin Shearing Kit	Covaris	Cat.No. 520127
NEB Next Ultra DNA Library prep kit	New England Biolabs	Cat No. NEB E7370S
KAPA Hyperprep Kit	Kappa Biosystems, Roche	Cat No. KK8504
<b>Deposited Data</b>		
Mass spectrometry	This paper	PXD014807
mm10 Blacklist	<a href="#">ENCODE Project Consortium, 2012</a>	<a href="http://mitra.stanford.edu/kundaje/akundaje/release/blacklists/mm10-mouse/mm10.blacklist.bed.gz">http://mitra.stanford.edu/kundaje/akundaje/release/blacklists/mm10-mouse/mm10.blacklist.bed.gz</a>
DNA sequencing: raw and analyzed data	This paper	GSE135029
EZH2 ChIPseq data	<a href="#">Marks et al., 2012</a>	GSM590133
<b>Experimental Models: Cell Lines</b>		
<i>M. musculus</i> : E14 mESCs	Laboratory of Kristian Helin	
<i>D. melanogaster</i> : S2-DRSC cells	Drosophila Genomics Resource Center; Stock No. 181	RRID:CVCL_Z992
<b>Oligonucleotides</b>		
NGS indexed PentAdapters	PentaBase	Cat No. SKU 310
<b>Software and Algorithms</b>		
Bowtie 2	<a href="#">Langmead and Salzberg, 2012</a>	<a href="https://github.com/BenLangmead/bowtie2">https://github.com/BenLangmead/bowtie2</a>
Trim Galore!	Babraham Bioinformatics	<a href="https://www.bioinformatics.babraham.ac.uk/projects/trim_galore/">https://www.bioinformatics.babraham.ac.uk/projects/trim_galore/</a> RRID:SCR_011847
SICER	<a href="#">Zang et al., 2009</a>	<a href="https://home.gwu.edu/~wpeng/Software.htm">https://home.gwu.edu/~wpeng/Software.htm</a> RRID:SCR_010843
R v3.2.1	R Project	<a href="https://www.r-project.org/">https://www.r-project.org/</a> RRID:SCR_001905
Seqmonk	Babraham Bioinformatics	<a href="https://www.bioinformatics.babraham.ac.uk/projects/seqmonk/">https://www.bioinformatics.babraham.ac.uk/projects/seqmonk/</a> RRID:SCR_001913
MATLAB 2017b (including the Statistics and Optimization Toolbox)	Mathworks	<a href="https://www.mathworks.com">https://www.mathworks.com</a>
AMICI	<a href="#">Fröhlich et al., 2017</a>	<a href="http://icb-dcm.github.io/AMICI/">http://icb-dcm.github.io/AMICI/</a>
PESTO	<a href="#">Stapor et al., 2018</a>	<a href="https://github.com/ICB-DCM/PESTO">https://github.com/ICB-DCM/PESTO</a>
Skyline	<a href="#">MacLean et al., 2010</a>	<a href="https://skyline.ms/project/home/begin.view?">https://skyline.ms/project/home/begin.view?</a>



## LEAD CONTACT AND MATERIALS AVAILABILITY

Further information and requests for resources and reagents should be directed to and will be fulfilled by the Lead Contact, Anja Groth ([anja.groth@bric.ku.dk](mailto:anja.groth@bric.ku.dk)).

This study did not generate new unique reagents.

## EXPERIMENTAL MODEL AND SUBJECT DETAILS

### E14 mESCs cell culture

E14 mESCs (male) were cultured at 37°C and 5% CO<sub>2</sub> on gelatin-coated plates in 2i/LIF medium (2i custom made medium (Thermo Fisher)) supplemented with Pen-Strep (GIBCO), 2mM Glutamax (GIBCO), 50  $\mu$ M  $\beta$ -mercaptoethanol (GIBCO), 0.1mM nonessential amino acids (GIBCO), 1mM sodium pyruvate (GIBCO), N2+B27 (Thermo Fisher), GSK3i (CHIR99021), MEKi (PD0325901), Leukemia Inhibitor Factor (LIF; produced in Kristian Helin laboratory). Medium was supplemented with light, medium or heavy arginine and lysine (R0 Arginine hydrochloride (Sigma A6969), R6 Arginine 13C6 (CNLM-2265-H1), R10 Arginine 13C6 15N4 (CNLM- 539-H1), K0 Lysine hydrochloride (Sigma L8662), K4 Lysine 4,4,5,5- d4 (DLM-2640-1 1gram), K8 Lysine 13C6 15N2 (CNLM-291-H-1 1gram) Cambridge isotope). We passaged cells every 2-3 days by removing the medium, washing cells in PBS, dissociating cells with 0.25% trypsin EDTA (GIBCO) with gentle disruption of colonies by pipetting, resuspending cells in medium, pelleting by centrifugation and resuspending cells and plating at density of 5x10<sup>6</sup> cells/15cm dish.

### Drosophila S2 Cell Culture

S2 cells (male) were grown in suspension in spinners in M3+BPYE media: Shields and Sang M3 Insect Medium (Sigma, S-8398), KHCO<sub>3</sub> (Sigma, 12602), yeast extract (Sigma, Y-1000), bactopectone (BD, 211705), 10% heat-inactivated FCS (GE Hyclone, SV30160.03) and 1X penicillin/streptomycin (GIBCO, 151400122). Cells were incubated at 25°C with 5% CO<sub>2</sub>.

### TIG3 K27M and TIG3K9M cell lines generation

Stable TIG3 cell lines expressing H3.3K27M or H3.3K9M were generated by lentiviral transduction. Briefly, lentiviral particles were produced by transfection of 293 FT cells with viral packaging (Pax8) and envelope (VSV) plasmids along with the appropriate vector containing the cDNA of interest (pCDH-EFI-MCS-IRES-PURO-H3.3K27M or pCDH-EFI-MCS-IRES-PURO-H3.3K9M). Virus-containing media was harvested after 48h and 1ml was used to infect TIG3 cells. Transduced cells were allowed to recover for 24h and then cultured under selection (1  $\mu$ g/mL Puromycin). Cells were harvested 8 days post transduction for immunoblot analysis. PCDH-EFI-MCS-IRES-PURO-H3.3K27M and pCDH-EFI-MCS-IRES-PURO-H3.3K9M plasmids were kindly provided by David Allis laboratory (The Rockefeller University, New York) and sequence verified.

### TIG3 K27M and TIG3K9M cell culture

TIG3 cells were grown in DMEM containing 10% FBS, 1% penicillin/streptomycin and 1  $\mu$ g/mL Puromycin. Medium was supplemented with MEM non-essential amino acid mix.

## METHOD DETAILS

### EZH2 inhibition and wash out

E14 mESCs were treated with 10  $\mu$ M of EPZ6438 EZH2 inhibitor (MedChem Express) for indicated time. For washout, cells were washed three times in PBS, trypsinized, washed in growth medium, and plated into R6K4 fresh medium.

### Sample preparation for histone modification analysis by MS

Acid extracted histones were resuspended in Lämmli buffer and separated by a 14%–20% gradient SDS-PAGE, stained with Coomassie (Brilliant blue G-250). Protein bands in the molecular weight range of histones (15–23 kDa) were excised as single band/fraction. Gel slices were destained in 50% acetonitrile/50mM ammonium bicarbonate. Lysine residues were chemically modified by propionylation for 30min at RT with 2.5% propionic anhydride (Sigma) in ammonium bicarbonate, pH 7.5 to prevent tryptic cleavage. This step added a propionyl group only to unmodified and monomethylated lysines, whereas lysines with other side chain modification will not obtain an additional propionyl-group. Subsequently, proteins were digested with 200ng of trypsin (Promega) in 50mM ammonium bicarbonate overnight and the supernatant was desalted by C18-Stagetips (reversed-phase resin) and carbon Top-Tips (Glygen) according to the manufacturer's instructions. Following carbon stage tip, the dried peptides were resuspended in 17  $\mu$ L of 0.1% TFA.

### LC-MS analysis of histone modifications

5  $\mu$ L of each sample were separated on a C18 home-made column (C18RP Reposil-Pur AQ, 120  $\times$  0.075mm  $\times$  2.4  $\mu$ m, 100Å, Dr. Maisch, Germany) with a gradient from 5% B to 30% B (solvent A 0.1% FA in water, solvent B 80% ACN, 0.1% FA in water) over 32min at a flow rate of 300nl/min (Ultimate 3000 RSLC Thermo-Fisher, San Jose, CA) and directly sprayed into a Q-Exactive HF mass spectrometer (Thermo-Fisher Scientific). The mass spectrometer was operated in the PRM mode to identify and quantify

specific fragment ions of N-terminal peptides of human histone 3.1 and histone 4 proteins. In this mode, the mass spectrometer automatically switched between one survey scan and 9 MS/MS acquisitions of the  $m/z$  values described in the inclusion list containing the precursor ions, modifications and fragmentation conditions (Table S1). Survey full scan MS spectra (from  $m/z$  250–800) were acquired with resolution 30,000 at  $m/z$  400 (AGC target of  $3 \times 10^6$ ). PRM spectra were acquired with resolution 15,000 to a target value of  $2 \times 10^5$ , maximum IT 60ms, isolation 2 window 0.7  $m/z$  and fragmented at 27% normalized collision energy. Typical mass spectrometric conditions were: spray voltage, 1.5kV; no sheath and auxiliary gas flow; heated capillary temperature, 250°C.

### Quantification of histone modifications

Data analysis was performed with Skyline (version 3.6) (MacLean et al., 2010) by using doubly and triply charged peptide masses for extracted ion chromatograms (XICs). Peaks were selected manually and the integrated peak values (Total Area MS1) were exported as .csv file for further calculations. The percentage of each modification within the same peptide is derived from the ratio of this structural modified peptide to the sum of all isotopically similar peptides. Therefore, the Total Area MS1 value was used to calculate the relative abundance of an observed modified peptide as percentage of the overall peptide. The unmodified peptide of histone 3.1 (aa 41–49) was used as indicator for total histone 3.1. Coeluting isobaric modifications were quantified using three unique MS2 fragment ions. Averaged integrals of these ions were used to calculate their respective contribution to the isobaric MS1 peak (e.g., H3K36me3 and H3K27me2K36me1). The mass spectrometry proteomics data have been deposited to the ProteomeXchange Consortium via the PRIDE partner repository with the dataset identifier PXD014807.

### ChIP-seq

Cells were grown for 7 days in 2i/LIF media supplemented with 10  $\mu$ M EZH2i (EPZ6438) or equivalent volume of DMSO. Cells were then processed using the truChIP Chromatin Shearing Kit (Covaris, 520127). In brief, cells were washed and fixed in 1% formaldehyde for 5 minutes. Crosslinking was quenched by adding Covaris quenching buffer and the reaction was incubated for 5 minutes. Fixed cells were washed twice in 1X PBS, scraped off in 1X PBS and spun down. Cell pellets were snap-frozen in liquid nitrogen, and stored at  $-80^\circ\text{C}$  until lysis. Nuclei isolation was performed on fixed cells following manufacturer's instructions. 20 million cells were sonicated in 1mL tubes using a Covaris M220 with the following settings: duty cycle 10% intensity, 200 cycles/ burst, 20 minutes processing time,  $7^\circ\text{C}$  bath temperature, water level full. Sonicated chromatin was centrifuged at 14,000 rpm at  $4^\circ\text{C}$  for 10 minutes and the supernatant was isolated for subsequent steps. In parallel, *Drosophila* S2 cells were fixed, lysed and sonicated as described above. For quantitative ChIP analysis of H3K36me2 and H3K27me3 input chromatin was mixed with *Drosophila* S2 chromatin (0.05% of total chromatin) after sonication. 30  $\mu$ g of mESCs sonicated chromatin or 30  $\mu$ g total of mixed mESCs and *Drosophila* S2 sonicated chromatin were diluted up to 500  $\mu$ L with dialysis buffer (4% glycerol, 10mM Tris-HCl, 1mM EDTA, 0.5mM EGTA; pH 8) and 400  $\mu$ L of incubation buffer (2.5% Triton X-100, 0.25% sodium deoxycholate, 0.25% SDS, 0.35M NaCl, 10mM Tris-HCl; pH 8) supplemented with leupeptin, aprotinin, pepstatin, and PMSF. Chromatin was pre-cleared with either Protein G agarose beads pre-coupled with bridging antibody (Active Motif #53017) following manufacturer's instruction (pG-Ab) or Protein A agarose beads for 1 hour at  $4^\circ\text{C}$ . After pre-clearing, chromatin was incubated overnight at  $4^\circ\text{C}$  with 10  $\mu$ g of the appropriate antibody (H3K27me1: Active Motif mAb #61015; H3K27me2: Cell Signaling mAb #9728; H3K27me3: Cell Signaling mAb #9733; H3K36me2: AbCam mAb #176921), followed by incubation for 3 hours with either pre-blocked Protein G-Ab or Protein A agarose beads (incubated in 1 mg/ml BSA in RIPA buffer overnight). Chromatin bound to beads was washed three times in RIPA buffer (140 mM NaCl, 10mM Tris-HCl, 1mM EDTA, 1% Triton X-100, 0.1% SDS, 0.1% sodium deoxycholate, 1mM PMSF; pH 8), four times in RIPA buffer with 0.5 M NaCl, once in LiCl buffer 3 (250mM LiCl, 10mM Tris-HCl, 1mM EDTA, 0.5% NP-40, 0.5% sodium deoxycholate; pH 8) and twice in TE (10mM Tris-HCl, 1mM EDTA; pH 8). Chromatin was incubated with 125  $\mu$ g/ml RNase A for 30 minutes at  $37^\circ\text{C}$  SDS was then added to a final concentration of 1% and samples were incubated with 250  $\mu$ g/ml proteinase K for 10 hours at  $37^\circ\text{C}$  followed by 6 hours incubation at  $65^\circ\text{C}$  for de-crosslinking. De-crosslinked DNA was purified and size selected with Agencourt AMPure XP beads (Beckman Coulter, A63881) by using first a 0.55:1 ratio followed by a 3:1 final ratio to obtain fragments between 200–700 bp. Finally, 10ng of purified DNA was subjected to end repair, A-tailing and amplification using the KAPA Hyperprep kit protocol (Roche, KK8504). Before and after amplification (7 PCR cycles) DNA was cleaned-up with Agencourt AMPure XP beads at a 0.8:1 ratio.

### Data sequencing, processing and analyses

ChIP-seq libraries were sequenced 75 bp single-end on an Illumina NextSeq 500. Trim Galore was used to trim adaptor sequences. Reads were mapped to the mm10 assembly mouse genome using Bowtie2 (Langmead and Salzberg, 2012). Reads with MAPQ < 20, PCR duplicates, and reads that overlapped with the Broad Institute sequencing blacklist (ENCODE Project Consortium, 2012) were filtered out. For downstream analyses, remaining reads were extended by 250bp. Reads were mapped to the dm3 assembly *Drosophila* genome using Bowtie2 (Langmead and Salzberg, 2012) to calculate reference-adjusted reads per million (RRPM) normalization factors. The number of uniquely mapped reads after deduplication was used to calculate RRPM as in (Reveron-Gomez et al., 2018). Fold change was calculated as the division of RRPM normalized signal of EZH2i treated samples by the RRPM normalized signal of DMSO treated samples and log transformed. Bedgraphs for screenshots and scatterplots were generated and visualized using Seqmonk (version 1.42.1). Boxplots were generated in R using custom scripts.

## Peak calling

Peak calls were created with SICER (Zang et al., 2009) using redundancy threshold = 1, window size = 500, fragment size = 250, effective genome fraction = 0.79, gap size = 1500 and an FDR threshold of 0.01. Input samples were used in peak calling to assess background and to determine true signal from IP enrichment.

## Mathematical modeling of histone tail methylation

The dynamics of combinatorial histone modifications of H3K27 and H3K36 have been modeled previously with systems of ordinary differential equations based on the assumption of mass action kinetics (Zheng et al., 2012). Here, we also employ ordinary differential equation models based on mass action kinetics and describe the observed modifications, which are averaged over all cells and histones of the individual generations (Figure 1A). We first describe the global model which includes demethylation, and then propose a different model that accounts for domains of specific modifications and that is able to explain data obtained in an inhibitor experiment (Figure 2D).

### Global model

The first model we considered consists of 45 state variables, with 15 state variables for each of the three generations (all possible combinations except K27me3K36me3) (Figure 2A). It describes the change in modifications due to methylation and demethylation as well as dilution, which occurs when the cells divide and new, unmodified histones are incorporated. This model is similar to the one proposed by (Zheng et al., 2012). To obtain a model for the relative abundance of modifications, we first derived the model for the absolute number of histone modifications. The ODE system for the absolute number of histone modifications  $\tilde{x}_g = (\tilde{x}_{g,00}, \dots, \tilde{x}_{g,23})$  reads for generation  $g = 1, 2, 3$

$$\begin{aligned} \dot{\tilde{x}}_{g,ij} = & \chi_{\{(i,j)=(0,0)\}}(i,j)c_g(t)N \\ & + \chi_{\{i>0 \wedge (i,j) \neq (3,3)\}}(i,j)k_{i-1j \rightarrow ij}\tilde{x}_{g,i-1j} \\ & + \chi_{\{j>0 \wedge (i,j) \neq (3,3)\}}(i,j)k_{ij-1 \rightarrow ij}\tilde{x}_{g,ij-1} \\ & - \chi_{\{i<3 \wedge (i,j) \neq (2,3)\}}(i,j)k_{ij \rightarrow i+1j}\tilde{x}_{g,ij} \\ & - \chi_{\{i<3 \wedge (i,j) \neq (3,2)\}}(i,j)k_{ij \rightarrow ij+1j}\tilde{x}_{g,ij} \\ & + \chi_{\{i<3 \wedge (i,j) \neq (2,3)\}}(i,j)d_{K27,i+1}\tilde{x}_{g,i+1j} \\ & + \chi_{\{j<3 \wedge (i,j) \neq (3,2)\}}(i,j)d_{K36,j+1}\tilde{x}_{g,ij+1} \\ & - \chi_{\{i>0 \wedge (i,j) \neq (3,3)\}}(i,j)d_{K27,i}\tilde{x}_{g,ij} \\ & - \chi_{\{j>0 \wedge (i,j) \neq (3,3)\}}(i,j)d_{K36,j}\tilde{x}_{g,ij} \\ \dot{N} = & cN. \end{aligned} \quad (1)$$

The indicator function is denoted by  $\chi$ ,  $k_{ij \rightarrow i+1j}$  is the rate constant for K27 methylation,  $k_{ij \rightarrow ij+1}$  is the rate constant for K36 methylation,  $i$  denotes the number of methyl groups at K27,  $j$  the number of methyl groups at K36,  $N(t) = N_0 e^{c(t-t_0)}$  the total number of histone tails with  $N(t_0) = N_0$  being the number of histone tails at the beginning of the experiment and  $c$  being the cell division rate. Furthermore,  $d_{K27,i}$  is the rate constant for demethylation, i.e., reducing the number of methyl groups at K27 from  $i$  to  $i-1$ . The special cases with  $(i,j) \neq (2,3)$  and  $(i,j) \neq (3,2)$  arise because we did not observe any K27me3K36me3 methylations. We model explicitly the three different generations of histones (Figure 1A). Newly incorporated histones are unmodified and belong to the generation of the corresponding culture medium (Figure 1A):

$$c_g(t) = \begin{cases} \chi_{\{t < -3h\}}(t)c & g=1. \\ \chi_{\{-3h \leq t < 0h\}}(t)c & g=2. \\ \chi_{\{t \geq 0h\}}(t)c & g=3. \end{cases} \quad \forall i,j. \quad (2)$$

The cell division rate  $c$  is multiplied with the number of histone tails in Equation 1, because the number of histone tails is proportional to the number of cells and thus duplicated at cell division. When changing the culture medium, initially no histones of this generation are present:

$$\tilde{x}_{g,ij}(t) = 0 \text{ for } \begin{cases} t < t_0 & g=1, \\ t < -3h & g=2, \\ t < 0h & g=3, \end{cases} \quad \forall i,j. \quad (3)$$

The model comprises  $n_\psi = 29$  parameters

$$\begin{aligned} \psi = & (c, d_{K27,1}, d_{K27,2}, d_{K27,3}, d_{K36,1}, d_{K36,2}, d_{K36,3}, k_{00 \rightarrow 01}, k_{00 \rightarrow 10}, k_{01 \rightarrow 02}, k_{01 \rightarrow 11}, k_{02 \rightarrow 03}, k_{02 \rightarrow 12}, \\ & k_{03 \rightarrow 13}, k_{10 \rightarrow 11}, k_{10 \rightarrow 20}, k_{11 \rightarrow 12}, k_{11 \rightarrow 21}, k_{12 \rightarrow 13}, k_{12 \rightarrow 22}, k_{13 \rightarrow 23}, k_{20 \rightarrow 21}, k_{20 \rightarrow 30}, k_{21 \rightarrow 22}, k_{21 \rightarrow 31}, \\ & k_{22 \rightarrow 23}, k_{22 \rightarrow 32}, k_{30 \rightarrow 31}, k_{31 \rightarrow 32}) \end{aligned}$$

which are required for the simulation of the observable. However, the relative weights are not independent and, thus, the model comprises only 28 independent parameters. To bring the system to relative scale, we divide the total abundance of modifications by the number of histone tails

$$x_{g,ij} = \frac{\tilde{x}_{g,ij}}{N}$$

$$\dot{x}_{g,ij} = \frac{\dot{\tilde{x}}_{g,ij}}{N} - \frac{\tilde{x}_{g,ij}\dot{N}}{N^2}.$$

This yields for the relative scale

$$\begin{aligned} \dot{\tilde{x}}_{g,ij} = & \chi_{\{(i,j)=(0,0)\}}(i,j)c_g(t) - c_g(t)\frac{\tilde{x}_{g,ij}}{N} + \chi_{\{i>0\wedge(i,j)\neq(3,3)\}}(i,j)k_{i-1j\rightarrow ij}\frac{\tilde{x}_{g,j-1j}}{N} \\ & + \chi_{\{j>0\wedge(i,j)\neq(3,3)\}}(i,j)k_{ij-1\rightarrow ij}\frac{\tilde{x}_{g,ij-1}}{N} - \chi_{\{i<3\wedge(i,j)\neq(2,3)\}}(i,j)k_{ij\rightarrow i+1j}\frac{\tilde{x}_{g,ij}}{N} \\ & - \chi_{\{j<3\wedge(i,j)\neq(3,2)\}}(i,j)k_{ij\rightarrow ij+1}\frac{\tilde{x}_{g,ij}}{N} + \chi_{\{i<3\wedge(i,j)\neq(2,3)\}}(i,j)d_{K27,j+1}\frac{\tilde{x}_{g,j+1j}}{N} \\ & + \chi_{\{j<3\wedge(i,j)\neq(3,2)\}}(i,j)d_{K36,j+1}\frac{\tilde{x}_{g,j+1j}}{N} - \chi_{\{i>0\wedge(i,j)\neq(3,3)\}}(i,j)d_{K27,j}\frac{\tilde{x}_{g,ij}}{N} \\ & - \chi_{\{j>0\wedge(i,j)\neq(3,3)\}}(i,j)d_{K36,j}\frac{\tilde{x}_{g,ij}}{N} \\ = & \chi_{\{(i,j)=(0,0)\}}(i,j)c_g(t) - c_g(t)x_{g,ij} + \chi_{\{i>0\wedge(i,j)\neq(3,3)\}}(i,j)k_{i-1j\rightarrow ij}x_{g,j-1j} \\ & + \chi_{\{j>0\wedge(i,j)\neq(3,3)\}}(i,j)k_{ij-1\rightarrow ij}x_{g,ij-1} - \chi_{\{i<3\wedge(i,j)\neq(2,3)\}}(i,j)k_{ij\rightarrow i+1j}x_{g,ij} \\ & - \chi_{\{j<3\wedge(i,j)\neq(3,2)\}}(i,j)k_{ij\rightarrow ij+1}x_{g,ij} + \chi_{\{i<3\wedge(i,j)\neq(2,3)\}}(i,j)d_{K27,j+1}x_{g,j+1j} \\ & + \chi_{\{j<3\wedge(i,j)\neq(3,2)\}}(i,j)d_{K36,j+1}x_{g,j+1j} - \chi_{\{i>0\wedge(i,j)\neq(3,3)\}}(i,j)d_{K27,j}x_{g,ij} \\ & - \chi_{\{j>0\wedge(i,j)\neq(3,3)\}}(i,j)d_{K36,j}x_{g,ij} \end{aligned}$$

for  $g=1,2,3$  and  $i,j=0,1,2,3$ . At relative scale, Equation 2 can be seen as the dilution that occurs due to cell division. The observables, i.e., the measurable output of the model, are the methylation ratios obtained by

$$y_{g,ij} = \frac{x_{g,ij}}{\sum_{i,j} x_{g,ij}}.$$

We assumed that methylation rates do not change for different culture media and different dynamics were obtained solely due to presence/absence of dilution (Equation 2) and different initial conditions (Equation 3).

### Domain model

As an alternative, we considered that demethylation of K27 and K36 does not exist. For this, we proposed a model which assumes that certain domains of the chromatin are determined to acquire certain methylation patterns, e.g., due to particular transcription factor binding or parental histone context. For example, histones of domain 00 do not get any methylations at all; histones of the domain 20 will get no additional methylations once the 20 state is reached; histones of the domain 31 can acquire the 31 methylation via different pathways (Figure 2B). The histone composition tends towards the state where all domains acquired their determined state. Since newly incorporated histones are unmodified (00), the model still shows dynamics. To construct this domain model, we denoted  $w_{lm}$  as the relative size of domain  $lm$ , with  $\sum_{l,m} w_{lm} = 1$ . Let  $x_{g,ij}^{lm}$  be the relative abundance of histone tails with methylation

K27meiK36mej in domain  $lm$  for generation  $g$ . Then the ODEs are

$$\dot{x}_{g,ij}^{lm} = \chi_{\{(i,j)=(0,0)\}}(i,j)c_g(t) - c_g(t)x_{g,ij}^{lm} + \chi_{\{0<i\leq l\}}(i,j)k_{i-1j\rightarrow ij}x_{g,j-1j}^{lm} + \chi_{\{0<j\leq m\}}(i,j)k_{ij-1\rightarrow ij}x_{g,ij-1}^{lm} - \chi_{\{i<l\}}(i,j)k_{ij\rightarrow i+1j}x_{g,ij}^{lm} - \chi_{\{j<m\}}(i,j)k_{ij\rightarrow ij+1}x_{g,ij}^{lm}$$

with  $c_g(t)$  as defined in Equation 2 and initial conditions

$$x_{g,ij}^{lm}(t) = 0 \text{ for } \begin{cases} t < t_0 & g=1, \\ t < -3h & g=2, \\ t < 0h & g=3, \end{cases} \quad \forall i,j,l,m. \quad (4)$$

The observables are obtained by

$$y_{g,ij} = \frac{\sum_{l,m} w_{lm} x_{g,ij}^{lm}}{\sum_{l,m} w_{lm} \sum_{i,j} x_{g,ij}^{lm}}.$$

We assumed that the methylation rate constants are shared between the domains, and estimated them together with the relative sizes of the domains from the data. The model comprises  $n_\psi = 38$  parameters

$$\begin{aligned} \psi = & (C, k_{00 \rightarrow 01}, k_{00 \rightarrow 10}, k_{01 \rightarrow 02}, k_{01 \rightarrow 11}, k_{02 \rightarrow 03}, k_{02 \rightarrow 12}, k_{03 \rightarrow 13}, k_{10 \rightarrow 11}, k_{10 \rightarrow 20}, k_{11 \rightarrow 12}, k_{11 \rightarrow 21}, \\ & k_{12 \rightarrow 13}, k_{12 \rightarrow 22}, k_{13 \rightarrow 23}, k_{20 \rightarrow 21}, k_{20 \rightarrow 30}, k_{21 \rightarrow 22}, k_{21 \rightarrow 31}, k_{22 \rightarrow 23}, k_{22 \rightarrow 32}, k_{30 \rightarrow 31}, k_{31 \rightarrow 32}, \\ & W_{00}, W_{01}, W_{02}, W_{03}, W_{10}, W_{11}, W_{12}, W_{13}, W_{20}, W_{21}, W_{22}, W_{23}, W_{30}, W_{31}, W_{32}) \end{aligned}$$

which are required for the simulation of the observable.

### Model calibration

Experimental measurements are generally noise corrupted and the model needs to take this into account. It has been shown that often a Laplace measurement noise model outperforms a Gaussian noise model (Maier et al., 2017). Therefore, we first compared the Gaussian and Laplace distributed measurement noise model. We compared the model output and the observables on a log-scale and offsetted both to cope with zero measurements

$$\log(\bar{y}_{g,jj} + \text{offset}) \sim p\left(\log(\bar{y}_{g,jj} + \text{offset}) \mid \log(y_{g,jj} + \text{offset}), \sigma\right), \quad (5)$$

with noise distribution  $p$ . The model parameters, including methylation rate constants, cell cycle and measurement noise, are comprised in the parameter vector  $\theta$ . The measurement for the time point indexed by  $k$  is denoted by  $\bar{y}_{g,jj}^k$ . The log-likelihood assuming Gaussian noise is given by

$$\log L(\theta) = \log L_D(\theta) = -\frac{1}{2} \sum_{g,j,j,k} \left( \log(2\pi\sigma^2) + \left( \frac{\log(\bar{y}_{g,jj}^k + \text{offset}) - \log(y_{g,jj}(t_k, \theta) + \text{offset})}{\sigma} \right)^2 \right) \quad (6)$$

and for the Laplace noise by

$$\log L(\theta) = \sum_{g,j,j,k} \left( \log(2\sigma) + \frac{\left| \log(\bar{y}_{g,jj}^k + \text{offset}) - \log(y_{g,jj}(t_k, \theta) + \text{offset}) \right|}{\sigma} \right). \quad (7)$$

Since we did not have prior information as our predicted domains do not correspond to steady state measurements and cannot be observed in a population of cycling cells, we used a maximum likelihood approach. The optimal parameters are obtained by maximizing the likelihood function, yielding the maximum likelihood estimate (MLE)  $\hat{\theta}$ . Maximum likelihood estimation was performed using the parameter estimation toolbox PESTO (Stapor et al., 2018), which provides an interface to the MATLAB function *fmincon*. For numerical reasons, we transformed parameters which are supposed to be positive to a logarithmic scale (Hass et al., 2019). The models were simulated using AMICI (Fröhlich et al., 2017), which provides an interface to the SUNDIALS solver suite (Hindmarsh et al., 2005). For model comparison, we employed the Bayesian Information Criterion (BIC) (Schwarz, 1978). The BIC value for model indexed by  $m$  is

$$\text{BIC}_m = -2\log L(\hat{\theta}_m) + \log(n_D)n\theta_m, \quad (8)$$

with  $n_D$  data points. The BIC rewards good likelihood values and penalizes the number of parameters. We chose  $\text{offset} = 10^{-1}$  which provided the best fit with respect to the QQ-plots for the global model and the domain model with 15 domains using Laplace noise (Figures S2A and S2B). We performed 100 local optimization runs for Gaussian and Laplace noise using the hierarchical approach for optimization proposed by Loos et al. (Loos et al., 2018). For the hierarchical approach, we analytically calculated the measurement noise parameter  $\sigma$ , which is shared for all time points, observables and generations. The hierarchical approach outperformed the standard approach for optimization. We found strong support for Laplace noise over Gaussian noise for both models ( $\Delta\text{BIC} > 600$ ). Both models were able to describe the data from untreated cells well (Figures 2C, S2C, and S2D). However, a model without demethylation for K27 was not able to describe, e.g., levels of K27me3K36me0 or K27me3K36m1 (Figure S2C). Since only the domain model is able to explain inhibitor experiments (Figure 2E), we reject the global model for the description of K27K36 dynamics.

### Model reduction and averaging

We did not expect all 15 domains to be necessary to explain the data and thus the domain model could be overparametrized. Since it was unclear which domains exist *a priori*, we performed model selection to detect the present domains. If we consider all potential combinations of domains, we would end up with  $2^{15}$  models, which is computationally too expensive. Performing a combination of



forward-selection and backward-elimination, we found eight domains 01, 02, 03, 13, 21, 23, 30, 32 which were necessary to explain the data. To be robust against the precise choice of domains, we performed model averaging over all models which were calibrated in the process of model reduction. For this, the BIC weight,

$$\omega_s = \frac{e^{-\frac{1}{2}BIC_s}}{\sum_{s=1}^{n_M} e^{-\frac{1}{2}BIC_s}}, \quad (9)$$

of each of the  $n_M = 137$  models was employed (Figure S2H). Since the rates are not comparable across models due to different domains, we analyzed the fluxes, which are the product of the abundance of the state and the methylation rate constant

$$\begin{aligned} \text{flux}_{ij \rightarrow i+1j} &= \sum_{l=0}^{i+1} \sum_{m=0}^i x_{1,ij}^{lm}(t_0) k_{ij \rightarrow i+1j}, \\ \text{flux}_{ij \rightarrow ij+1} &= \sum_{l=0}^i \sum_{m=0}^{j+1} x_{1,ij}^{lm}(t_0) k_{ij \rightarrow ij+1}. \end{aligned}$$

The fluxes shown in Figure 2F are model averaged using the BIC weights (Equation 9) (Wasserman, 2000).

### Model prediction and validation

To further test and validate the models, we used the data of the inhibitor experiment. Using our calibrated models, we predicted the total amount of K27me3 in generation 1 under inhibitor treatment (Figure 2D). For this, we assumed that the tri-methylation rates were inhibited by a factor  $\kappa$ :

$$k_{2j \rightarrow 3j, \text{inh}} = (1 - \kappa) k_{2j \rightarrow 3j, \text{untr}}. \quad (10)$$

To obtain reasonable values for  $\kappa$ , we analyzed a simplified model which only considers K27 methylations of histones of generation 3,  $X_0, X_1, X_2, X_3$  for un-, mono-, di-, and tri-methylation at K27 and assumed independence between the methylation sites. The model reads

$$\begin{aligned} \dot{X}_0 &= c - cX_0 - k_{0 \rightarrow 1}X_0 + d_{K27,1}X_1, \\ \dot{X}_1 &= -cX_1 + k_{0 \rightarrow 1}X_0 - k_{1 \rightarrow 2}X_1 + d_{K27,2}X_2 - d_{K27,1}X_1, \\ \dot{X}_2 &= -cX_2 + k_{1 \rightarrow 2}X_1 - k_{2 \rightarrow 3}X_2 + d_{K27,3}X_3 - d_{K27,2}X_2, \\ \dot{X}_3 &= -cX_3 + k_{2 \rightarrow 3}X_2 - d_{K27,3}X_3. \end{aligned}$$

The steady states for K27me3 for untreated cells and cells in the inhibitory experiment are given by

$$X_{3, \text{untr}} = \frac{k_{2 \rightarrow 3}X_{2, \text{untr}}}{d_{K27,3} + c}, \quad (11)$$

$$X_{3, \text{inh}} = \frac{(1 - \kappa)k_{2 \rightarrow 3}X_{2, \text{inh}}}{d_{K27,3} + c}. \quad (12)$$

Thus, K27me3 only depends on the tri-methylation rate constant  $k_{2 \rightarrow 3}$ , the demethylation rate constant  $d_{K27,3}$ , the dilution rate constant  $c$ , the amount of relative K27me2 and in the inhibitor case the factor  $\kappa$  (Equation 10) by which the tri-methylation is inhibited (Figure S2E). Thus, we obtained

$$\frac{d_{K27,3} + c}{k_{2 \rightarrow 3}} = \frac{X_{2, \text{untr}}}{X_{3, \text{untr}}} = (1 - \kappa) \frac{X_{2, \text{inh}}}{X_{3, \text{inh}}} \quad (13)$$

$$\Rightarrow \kappa = 1 - \frac{X_{2, \text{untr}}X_{3, \text{inh}}}{X_{3, \text{untr}}X_{2, \text{inh}}}. \quad (14)$$

Using the last time point for generation 3 from data  $D_{\text{inh}}$ , we obtained for three replicates a rough estimate  $\kappa = 0.928 \pm 0.052$  (Figure S2G). The same expression for  $\kappa$  (Equation 14) is also valid for the domain model. We compared our model predictions to the experimental data for K27me3 levels, i.e., summing all states with K27me3, to be robust against potential effects of the inhibitor on K36 methylations. We only assumed the tri-methylation rate to change. However, if also mono-, or di-methylation changes, the model predictions would be even lower and the illustrated predictions in Figure 2E can be seen as rough estimates for the upper bound.

### Modeling differences between generation 2 histones in untreated and recovery experiments

For all further analyses, we used a domain model with eight domains (01,02,03,13,21,23,30,32). To detect differences between generation 2 histones of untreated and recovering cells, we performed a forward selection to find the most substantial changes in rate constants. In the first step of forward selection, only changes in the rate constants  $k_{00 \rightarrow 10}$  and  $k_{20 \rightarrow 30}$  yield substantial improvements with  $\Delta\text{BIC} < 10$ . Allowing the rate constant for  $k_{00 \rightarrow 10}$  to differ yields the biggest improvement in BIC values, and this rate constant is estimated to be roughly halved (0.47) in cells lacking K27me3. Overall, the model allowing for differences in  $k_{00 \rightarrow 10}$ ,  $k_{00 \rightarrow 01}$ ,  $k_{20 \rightarrow 21}$  and  $k_{20 \rightarrow 30}$  has the lowest BIC and thus the highest quality (Figures 3E and 3F).

### Implementation

The MATLAB code used for the analysis of the manuscript is made available via Zenodo (<https://zenodo.org/record/3353481>). The toolboxes used for the ODE simulation (AMICI) and parameter estimation (PESTO) are both available under <https://github.com/ICB-DCM>. The analysis was performed with MATLAB 2017b.

### QUANTIFICATION AND STATISTICAL ANALYSIS

Figure 1:  $6 \leq n \leq 9$  biological replicates have been performed. Figure 2D and 2E: 3 biological replicates have been performed. Figures 3 and 4A–4C: 3 biological replicates have been performed. Figures 4: 2 biological replicates have been performed. The mean with standard deviation is shown.

### DATA AND CODE AVAILABILITY

The mass spectrometry dataset generated during this study is available at Pride:PXD014807. The sequencing datasets generated during this study are available at GEO:GSE135029. The MATLAB code used for the mechanistic modeling is available at Zenodo [<https://zenodo.org/record/3353481>]. The publicly available EZH2 data reported in this paper is available at GEO:GSM590133.

**Cell Reports, Volume 30**

## **Supplemental Information**

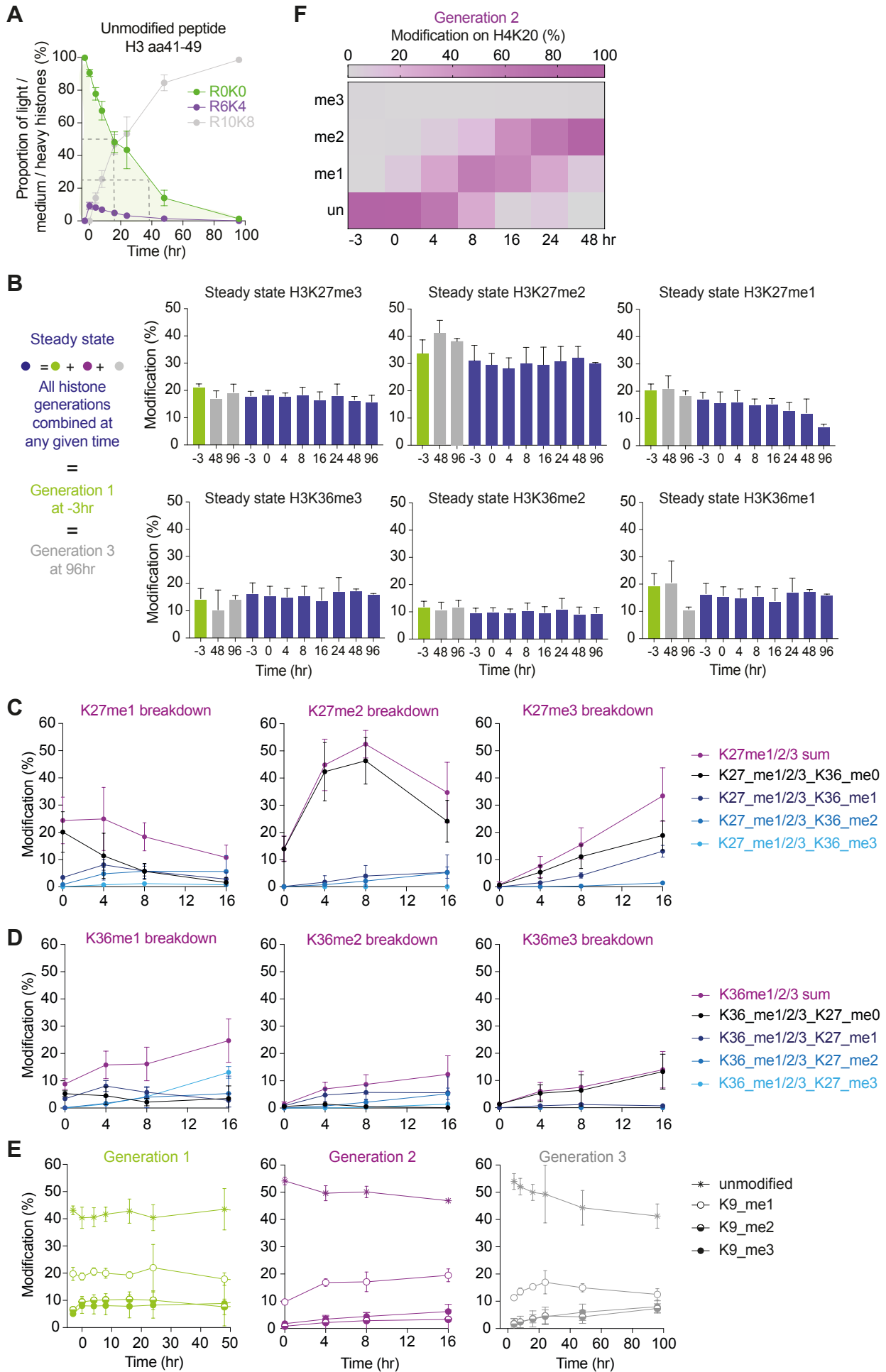
### **Domain Model Explains Propagation**

### **Dynamics and Stability of Histone H3K27**

### **and H3K36 Methylation Landscapes**

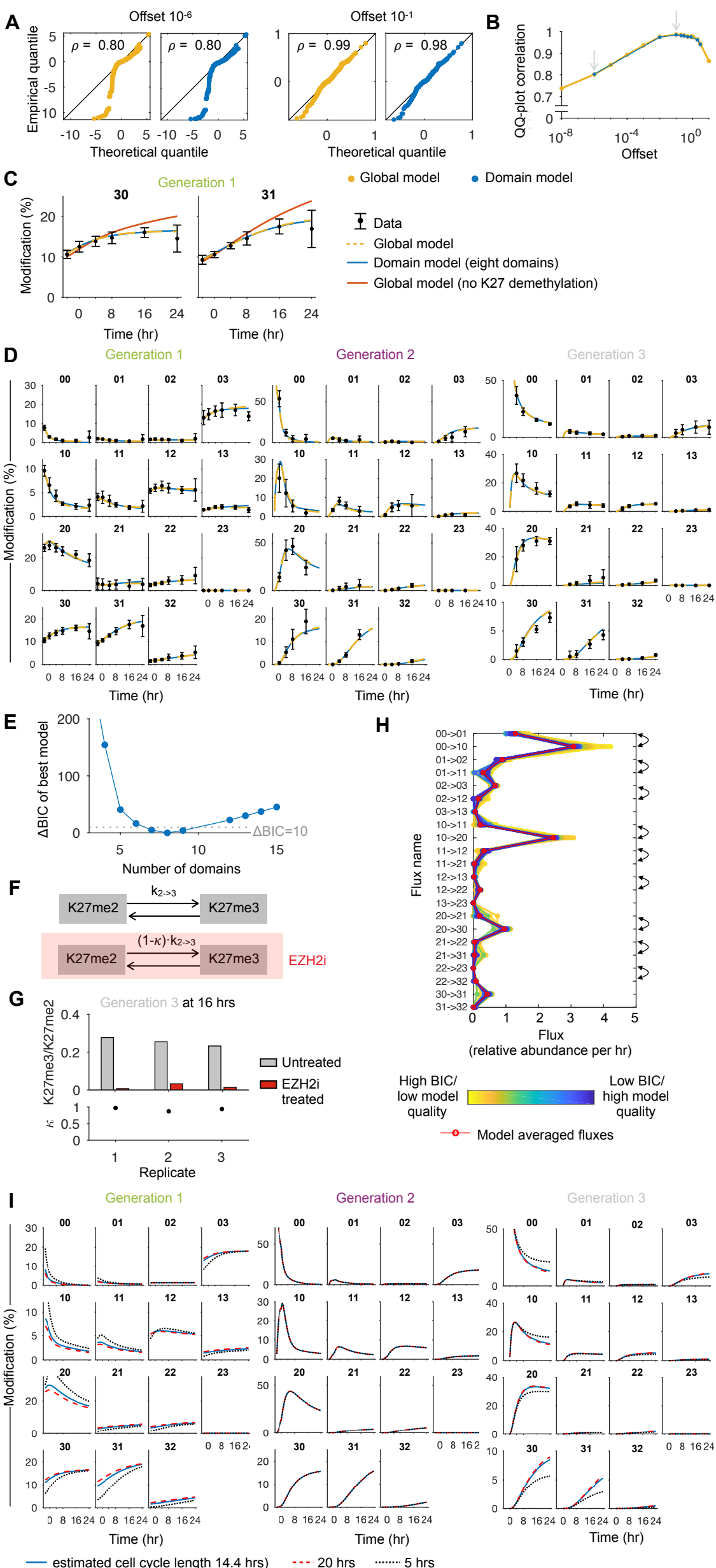
**Constance Alabert, Carolin Loos, Moritz Voelker-Albert, Simona Graziano, Ignasi Forné, Nazaret Reveron-Gomez, Lea Schuh, Jan Hasenauer, Carsten Marr, Axel Imhof, and Anja Groth**

**Figure S1**



**Figure S1, related to Figure 1.** **A.** Proportion of each histone generations across the time course, based on quantification of the H3 aa41-49 peptide that remains unmodified. The proportion is given as a percentage such that the sum equals 100 % at any given time. **B.** Total modification levels across the time course, represented by pre-existing histones (green), combinations of the different generations (blue) and third generation histones (grey). For each modification, the sum is given (e.g. for K27me3 is given as the sum of K27me3K36me0, K27me3K36me1, K27me3K36me2, and K27me3K36me3). **C, D.** Methylation levels on generation 2 histones for K27 and K36, on all individual peptides used to generate the sum shown in Fig. 1D. **E.** Methylation levels on histone generations 1, 2 and 3 for H3K9. (un) unmodified; (me1) mono-methylated; (me2) di-methylated; (me3) tri-methylated. **F.** Heatmap showing stepwise methylation of H4K20 methylation on generation 2 histones. (un) Unmodified; (me1) mono-methylated; (me2) di-methylated; (me3) tri-methylated.



**Figure S2**

**Figure S2, related to Figure 2.** **A.** Comparing different offsets by which data and model simulation are shifted shows highest QQ correlations for  $10^{-1}$ . **B.** Correlation for the QQ-plots for varying offsets. The maximum correlation is achieved for offset  $10^{-1}$ . **C.** Model fits including the global model without K27 demethylation for K27me3K36me0 and K27me3K36me1. The models were calibrated for the full data set. **D.** Both the global and the domain model is able to fit methylation dynamics in all generations. **E.** Model reduction for the domain model. The difference in BIC values is shown for the best tested model with given numbers of domains. A model with 8 domains has the best Bayesian Information Criterion (BIC) value, and there are models with 7 and 9 domains which cannot be rejected according to their BIC value. The dotted line shows the threshold of  $\Delta\text{BIC}=10$ . **F.** Illustration of the parametrization for the efficiency  $\kappa$  of the inhibitor. **G.** Estimates for  $\kappa$  comparing K27me3 and K27me2 levels for generation 3 histones for untreated cells and cells with EZH2 inhibitor. **H.** Fluxes obtained with the maximum likelihood estimates (MLEs) for all calibrated models. The models are color coded according to their BIC value. The model averaged (using BIC weights) fluxes are highlighted with red and fluxes which are compared in Fig. 2F are highlighted by arrows. **I.** Prediction of methylation dynamics for varying cell cycle lengths using the domain model. The blue line indicates the model for the estimated cell cycle length of 14.4 hrs. For a faster cell cycle (5 hrs, black dotted line), the model predicts overall a higher relative abundance of the lower methylated states, while for a slower cell cycle (20 hrs, red dashed line) the overall relative methylation slightly increases. The initial methylation abundances for generation 1 histones differ for the cell cycle lengths, but approach the same steady state when the cell cycle does not affect the dynamics anymore (after 0 hr). For histones of generation 2, the cell cycle length only has an influence during the 3 hrs labeling time and, therefore, the differences for different cell cycle lengths are minor. Histones of generation 3 approach different population steady states for varying cell cycle lengths.

**Figure S3**

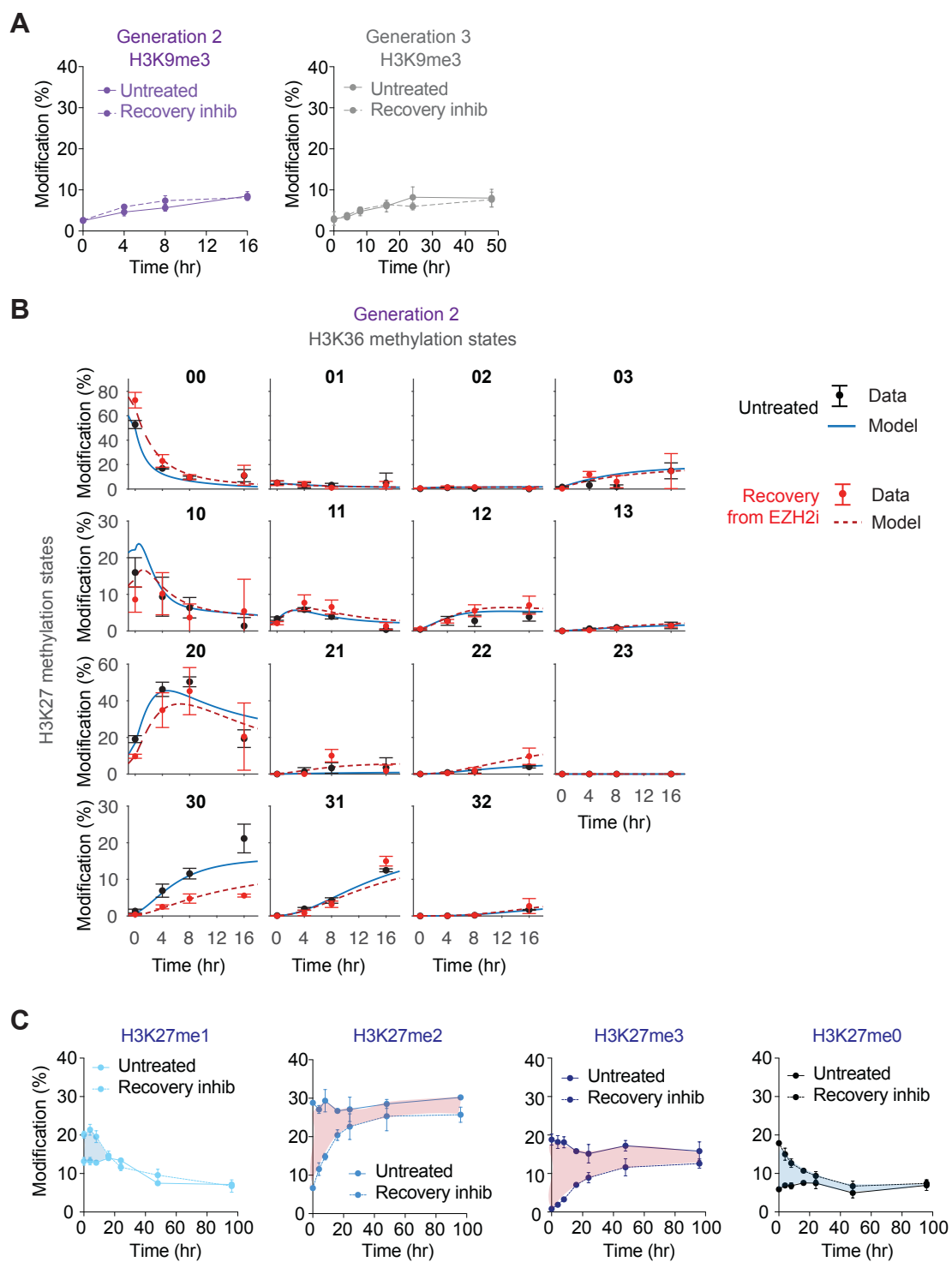
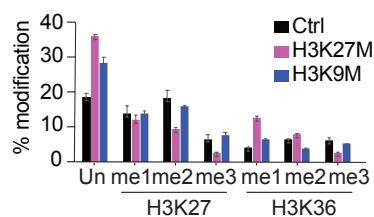


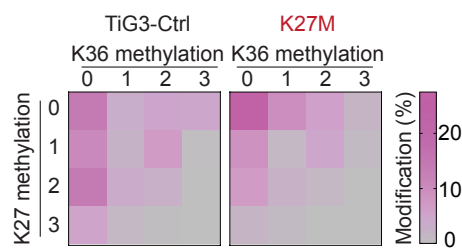
**Figure S3, related to Figure 3.** **A.** H3K9me3 levels on generation 2 and 3 histones. Experimental design as described in Fig. 3B. **B.** K27 and K36 methylation levels on generation 2 histones for untreated cells and during recovery. Experimental measurements and the model fit allowing for differences in the methylation rate constants  $k_{00 \rightarrow 01}$ ,  $k_{00 \rightarrow 10}$ ,  $k_{20 \rightarrow 21}$  and  $k_{20 \rightarrow 30}$  are shown. **C.** Total methylation levels on K27 across the time course on the combination of all three histone generations calculated as in Fig. S1B. Losses and gains compared to untreated control are by pink and blue shaded areas, respectively.

**Figure S4**

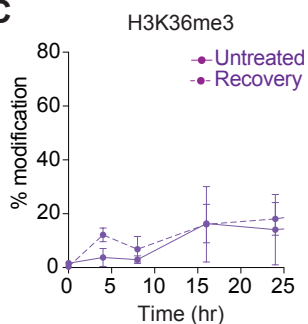
**A**



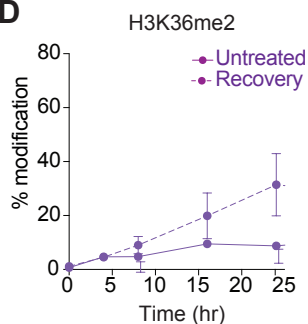
**B**



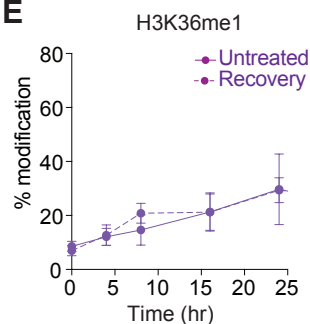
**C**



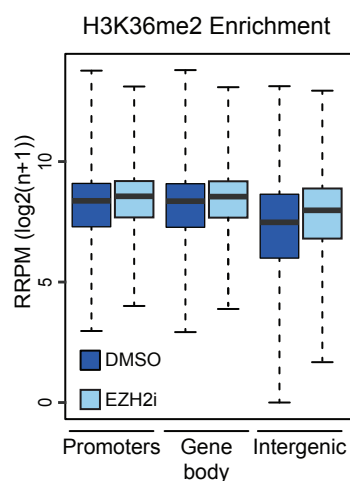
**D**



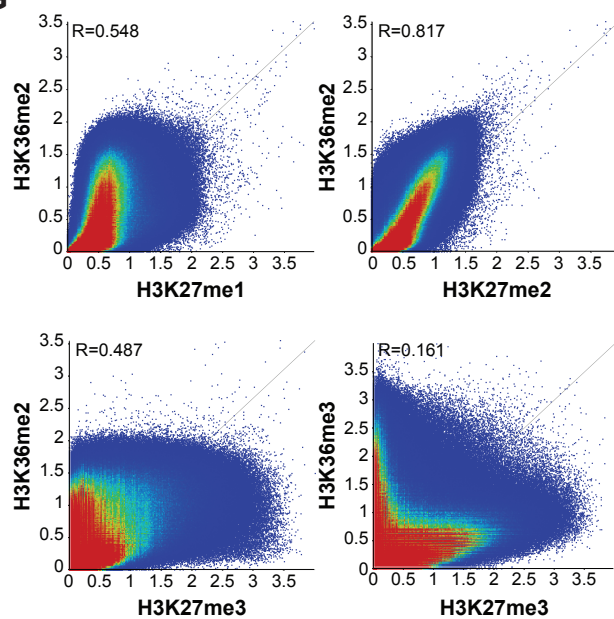
**E**



**F**



**G**



**H**

**H3K36me2 Enrichment at K27me3 domains**

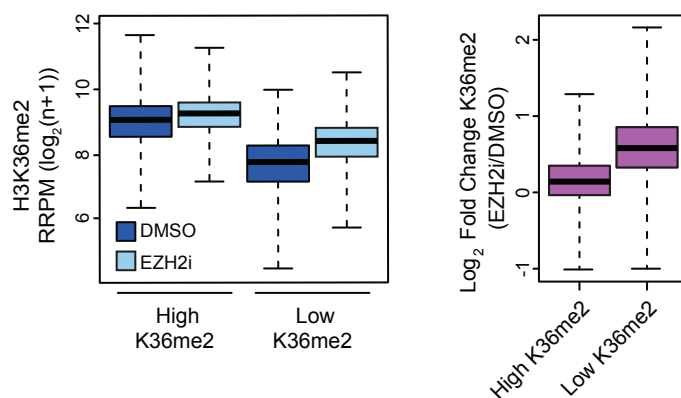




**Figure S4, related to Figure 4.** **A.** Bar-diagram showing H3K27 and H3K36 methylation levels in TIG-3 cells expressing H3K27M and H3K9M and untransduced controls (Ctrl). **B.** Heatmap showing H3K27 and H3K36 methylation levels in TIG-3 cells expressing H3K27M compare to control (Ctrl). **C-E.** H3K36 methylation levels on generation 2 histones in untreated conditions and upon recovery from EZH2 inhibitor treatment. **F.** Boxplot of H3K36me2 ChIP-seq signal over 1kb windows across promoters, gene bodies and intergenic regions. Black line, median; dashed lines,  $1.5 \times$  interquartile range. Quantitated with RRPM,  $\log_2(n + 1)$ . **G.** Scatterplots showing direct comparison of ChIP-seq signal over 1kb windows across the genome for the indicated pairs of histone modifications. Quantitated with RPM,  $\log_2(n+1)$ . Pearson's correlation R value for each plot is shown. **H.** Boxplot of H3K36me2 ChIP-seq signal over 1kb windows across H3K27me3 domains overlapping (high K36me2) or not overlapping (low K36me2) K36me2 peaks. Black line, median; dashed lines,  $1.5 \times$  interquartile range. Quantitated with RRPM,  $\log_2(n + 1)$ .

**Supplemental Table 1, related to STAR method, LC-MS analysis of histone modifications.**

Mass [m/z]	Formula [M]	Formula type	Species	CS [z]	Polarity	Start [min]	End [min]	(N)CE	(N)CE type	MSX ID	Comment
539.3141				3	Positive	35	45	29	NCE		H3_27_40_K27K36K37_m1pp + H3_27_40_K27K36K37_pm1p_light
545.346				3	Positive	35	45	29	NCE		H3_27_40_K27K36K37_m1pp + H3_27_40_K27K36K37_pm1p_medium
550.6644				3	Positive	35	45	29	NCE		H3_27_40_K27K36K37_m1pp + H3_27_40_K27K36K37_pm1p_heavy
529.9825				3	Positive	30	40	30	NCE		H3_27_40_K27K36K37_m2m1p + H3_27_40_K27K36K37_pm3p_light
536.0143				3	Positive	30	40	30	NCE		H3_27_40_K27K36K37_m2m1p + H3_27_40_K27K36K37_pm3p_medium
541.3328				3	Positive	30	40	30	NCE		H3_27_40_K27K36K37_m2m1p + H3_27_40_K27K36K37_pm3p_heavy
534.6544				3	Positive	32	40	30	NCE		H3_27_40_K27S28K36K37_me3me1p + H3_27_40_K27S28K36K37_me1me3p_light
540.6862				3	Positive	32	40	30	NCE		H3_27_40_K27S28K36K37_me3me1p + H3_27_40_K27S28K36K37_me1me3p_medium
546.0047				3	Positive	32	40	30	NCE		H3_27_40_K27S28K36K37_me3me1p + H3_27_40_K27S28K36K37_me1me3p_heavy
525.3106				3	Positive	30	38	30	NCE		H3_27-40_K27K36K37_pme2p + H3_27-40_K27K36K37_me2pp_light
531.3424				3	Positive	30	38	30	NCE		H3_27-40_K27K36K37_pme2p + H3_27-40_K27K36K37_me2pp_medium
536.6609				3	Positive	30	38	30	NCE		H3_27-40_K27K36K37_pme2p + H3_27-40_K27K36K37_me2pp_heavy
520.6509				3	Positive	25	35	32	NCE		H3_27-40_K27K36K37_me2me3p + H3_27-40_K27K36K37_me3me2p_light
526.6827				3	Positive	25	35	32	NCE		H3_27-40_K27K36K37_me2me3p + H3_27-40_K27K36K37_me3me2p_medium
532.0011				3	Positive	25	35	32	NCE		H3_27-40_K27K36K37_me2me3p + H3_27-40_K27K36K37_me3me2p_heavy
543.986				3	Positive	34	42	30	NCE		H3_27_40_K27K36K37_m1m1p_light
550.0178				3	Positive	34	42	30	NCE		H3_27_40_K27K36K37_m1m1p_medium
555.3363				3	Positive	34	42	30	NCE		H3_27_40_K27K36K37_m1m1p_heavy